Received: 10 June 2024 | Revised: 20 March 2025 | Accepted: 21 May 2025

DOI: 10.1002/cac2.70038

CANCER COMMUNICATIONS Open Access

ORIGINAL ARTICLE

# Lipid metabolism reprograming by SREBP1-PCSK9 targeting sensitizes pancreatic cancer to immunochemotherapy

**Mengyi Lao**[1,2,3,4] | **Xiaozhen Zhang**[1,2,3] | **Zejun Li**[1,2,3] | **Kang Sun**[1,2,3] | **Hanshen Yang**[1,2,3] | **Sicheng Wang**[1,2,3] | **Lihong He**[1,2,3] | **Yan Chen**[1,2,3] | **Hanjia Zhang**[1,2,3] | **Jiatao Shi**[1,2,3] | **Daqian Xu**[1,2,5] | **Tingbo Liang**[1,2,3] | **Xueli Bai**[1,2,3]

[1]Department of Hepatobiliary and Pancreatic Surgery, the First Affiliated Hospital, School of Medicine, Zhejiang University, Hangzhou, Zhejiang, P. R. China

[2]Zhejiang Provincial Key Laboratory of Pancreatic Disease, the First Affiliated Hospital, School of Medicine, Zhejiang University, Hangzhou, Zhejiang, P. R. China

[3]Cancer Center, Zhejiang University, Hangzhou, Zhejiang, P. R. China

[4]Department of Breast Surgery, the First Affiliated Hospital, School of Medicine, Zhejiang University, Hangzhou, Zhejiang, P. R. China

[5]Institute of Translational Medicine, Zhejiang University School of Medicine, Hangzhou, Zhejiang, P. R. China

**List of Abbreviations:** ACACA, acetyl-CoA carboxylase alpha; ACSL1, acyl-CoA synthetase long-chain family member 1; ACTB, $\beta$-actin; ANOVA, Analysis of Variance; AUC, Area under the curve; Baf-A1, bafilomycin-A1; BCA, bicinchoninic acid; CAF, cancer-associated fibroblast; CCK-8, cell counting kit-8.; CD, chow diet; CFDA, China Food and Drug Administration; ChIP, chromatin immunoprecipitation; CHX, cycloheximide; CMV, cytomegalovirus; Co-IP, Co-immunoprecipitation; CTLA4, cytotoxic T-lymphocyte associated protein 4; CUT & Tag, Cleavage Under Targets and Tagmentation; DAPI, 2- (4-Amidinophenyl)-6-indolecarbamidine dihydrochloride; DDT, dithiothreitol; DMEM, Dulbecco's modified Eagle's medium; ELISA, enzyme-linked immunosorbent assay; FABP4, fatty acid-binding protein 4; FASN, fatty acid synthase; FBS, fetal bovine serum; FC, fold change; Foxp3, forkhead box P3; FPKM, fragments per kilobase of exon model per million mapped fragments; GAPDH, glyceraldehyde-3-phosphate dehydrogenase; GC-MS, gas chromatography-mass spectrometry; GEM, gemcitabine; GEMM-KTC, LSL-*Kras*$^{G12D/+}$;TgfbRfl/+; Ptfla-cre driven spontaneous PDAC; GO, gene ontology; GSEA, Gene Set Enrichment Analysis; GST, glutathione S-transferase; GZMB, granzyme B; HDL, high-density lipoprotein; HFD, high-fat diet; HIF-1; NF-$\kappa$B, hypoxia inducible factor-1; nuclear factor kappa-B; IAA, iodoacetamide; ICB, Immune checkpoint blockade; IF, immunofluorescence; IFN-$\gamma$, interferon gamma; IHC, immunohistochemistry analysis; IL-2, interleukin 2; IQR, interquartile range; KEGG, Kyoto Encyclopedia of Genes and Genomes; KPC, LSL-*Kras*$^{G12D/+}$; LAMP2, lysosome - associated membrane protein 2; LC, liquid chromatography; LDL, low-density lipoprotein; LSL-*Trp53*$^{R172H/+}$, ; mAbs, monoclonal antibodies; MGST1, microsomal glutathione S-transferase 1; MHC- I, major histocompatibility complex class I; mIHC, multiplexed IHC; MS, mass spectrometry; MSigDB, molecular signatures; OE, overexpression; OPLS-DA, orthogonal partial least-squares discriminant analysis; OS, overall survival; pan-CK, pan Cytokeratin; PBS, phosphate-buffered saline; PCA, principal component analysis; PCSK9, proprotein convertase subtilisin/kexin type 9; PD-1, programmed death receptor 1; PDAC, pancreatic ductal adenocarcinoma; PD-L1, programmed cell death 1 ligand 1; PDX, patient-derived xenograft; *Pdx1*-Cre, ; , *Ptfla*-cre driven spontaneous PDAC; PVDF, polyvinylidene fluoride; qRT-PCR, quantitative reverse transcription polymerase chain reaction; RECIST, Response Evaluation Criteria in Solid Tumors version 1.1; RIPA, radioimmunoprecipitation assay; RNA-Seq, RNA-sequencing; ROC, receiver operating characteristic; SCAP, SREBP cleavage activating protein; SCD1, stearoyl-CoA desaturase 1; SD, standard deviation; shRNAs, short hairpin RNAs; siRNAs, small interfering RNAs; SPF, specific pathogen-free; SREBF1, sterol regulatory element binding transcription factor 1; SREBP1, sterol regulatory element binding proteins 1; STAT3, signal transducer and activator of transcription; TAMs, tumor-associated macrophages; TC, total cholesterol; TC, total cholesterol; TCGA, the Cancer Genome Atlas Network; *Tgfb*$^{Rfl/+}$, ; TILs, tumor-infiltrating lymphocytes; TIME, tumor immunity in the microenvironment; TIMER, Tumor Immune Estimation Resource; TME, tumor microenvironment; TNF-$\alpha$, tumor necrosis factor alpha; WAG, wheat germ agglutinin.

Mengyi Lao and Xiaozhen Zhang contributed equally

**Correspondence**
Xueli Bai and Tingbo Liang, Department of Hepatobiliary and Pancreatic Surgery, the First Affiliated Hospital, Zhejiang University School of Medicine, 79 Qingchun Road, Hangzhou 310009, Zhejiang, P. R. China.
Email: shirleybai@zju.edu.cn and liangtingbo@zju.edu.cn

**Funding information**
National Natural Science Foundation of China, Grant/Award Numbers: 81830089, 82071867, 82188102, 82403852, U20A20378, U23A20462

## Abstract

**Background:** Pancreatic cancer's aberrant lipid metabolism fuels cell growth, invasion, and metastasis, yet its impact on immune surveillance and immunotherapy is unclear. This study investigated how sterol regulatory element-binding transcription factor 1 (SREBP1)-driven lipid metabolism affects the tumor microenvironment (TME) in pancreatic ductal adenocarcinoma (PDAC).

**Methods:** Clinical significance of SREBP1 was assessed in a PDAC cohort from China and The Cancer Genome Atlas (TCGA) cohorts. The in vitro mechanisms that SREBP1 regulated programmed cell death-ligand 1 (PD-L1) and proprotein convertase subtilisin/kexin type 9 (PCSK9) were investigated using immunofluorescence, flow cytometry, Western blotting, luciferase assays and chromatin immunoprecipitation. In vivo studies using PDAC-bearing mice, humanized patient-derived tumor xenograft (PDX) models, and autochthonous model of mutation (GEMM-KTC) evaluated the efficacy and mechanisms of programmed death receptor 1 (PD-1) antibodies and lipid inhibitors.

**Results:** Patients responding to anti-PD-1 therapy exhibited lower serum lipid levels than non-responders. Targeting SREBP1 disrupted lipid metabolism, decelerated tumor growth, and boosted the efficacy of immunotherapy for PDAC. Mechanistically, SREBP1 directly bound the PD-L1 promoter, suppressing its transcription. Meanwhile, PCSK9, a direct transcriptional target of SREBP1, modulated PD-L1 levels via lysosomal degradation. Consequently, the combination of PCSK9-neutralizing antibodies with PD-1 monotherapy showed a robust antitumor effect in both humanized PDX and GEMM-KTC models.

**Conclusions:** The SREBP1-PCSK9 axis-mediated lipid metabolism is crucial for triggering immune evasion and resistance to anti-PD-1. Targeting the SREBP1-PCSK9 axis could potentially reverse PDAC's resistance to anti-PD-1 therapy.

**KEYWORDS**
Pancreatic ductal adenocarcinoma, lipid metabolism, immunochemotherapy, SREBP1, PCSK9, immunosuppressive tumor microenvironment, PD-1/PD-L1

## 1 | BACKGROUND

Pancreatic ductal adenocarcinoma (PDAC) is highly resistant to chemotherapy, targeted therapies, and even immunotherapy, often due to its dense desmoplasia and immunosuppressive tumor microenvironment (TME) [1]. Immune checkpoint blockade (ICB) therapy can lead to long-lasting tumor regression, but it is effective in only a small percentage of cancer patients, suggesting the presence of additional immunosuppressive mechanisms in the TME [2]. Therefore, elucidating the mechanisms behind TME-induced immunosuppression is essential for developing improved immunotherapeutic strategies and combination therapies.

Tumors can be categorized into four distinct tumor immune microenvironment (TIME) types based on the expression of programmed cell death 1 ligand 1 (PD-L1) and the infiltration of tumor-infiltrating lymphocytes (TILs): Type I (PD-L1$^-$/TIL$^-$); Type II (PD-L1$^+$/TIL$^+$); Type III (PD-L1$^-$/TIL$^+$); and Type IV (PD-L1$^+$/TIL$^-$) [3]. Patients with solid tumors of TIME Types I, III, and IV often have a reduced response to ICB therapy [3]. The abundant desmoplasia and the immunosuppressive TME in PDAC lead to most tumors being categorized as Types I and IV (low expression of PD-L1 and the absence of TILs). Thus, ICB therapy has had limited effectiveness in PDAC to date [4]. In theory, a promising therapeutic approach is to transform Types I, III, and IV tumors into Type II, enhancing the

potency of ICB in PDAC. Notably, tumoral PD-L1 expression serves as a crucial predictive biomarker for patient responsiveness to ICB treatment [5, 6]. Research continues to validate that increasing PD-L1 expression levels in cancer cells significantly boosts the effectiveness of ICB therapies across various tumor experimental models [7–9].

Oncogene-driven changes in tumor cell metabolism can impact the TME to limit immune responses and present barriers to cancer therapy [10]. Among the myriad of metabolic pathways, lipid metabolism, particularly fatty acid metabolism, is vital for cancer cell survival and growth. It significantly influences immune cell functions and differentiation, aiding in cancer's immune evasion [11]. Research suggests that targeting lipid metabolism in T cells and tumor-associated macrophages (TAMs) with specific drugs can enhance their responsiveness to ICB therapy [12–14]. Thus, targeting lipid metabolism reverses the suppressive TIME, maintains the antitumor function of TILs, and converts Types I, III, and IV into Type II, offering promising opportunities for cancer immunotherapy [15, 16].

Aberrant lipid metabolism in PDAC promotes cancer cell growth, invasion, and metastasis [17]. Sterol regulatory element binding transcription factor 1 (SREBP1) involved in lipid metabolism regulates multiple cancer pathways [18]; however, its role in the TIME and PDAC immunotherapy is unknown. To elucidate the effect and mechanism of targeting SREBP1 in sensitizing pancreatic cancer to immunochemotherapy, we conducted a comprehensive analysis based on the differential expression profiles of PDAC patients' samples. Additionally, we performed in vitro and in vivo assays to investigate the involvement of SREBP1 in the TME of PDAC. This study aimed to elucidate the clinical relevance of SREBP1 in PDAC and the molecular mechanisms underlying SREBP1-mediated lipid metabolism and its effects on the TME of PDAC.

## 2 | MATERIALS AND METHODS

### 2.1 | Human/mouse PDAC cells

Murine pancreatic ductal carcinoma cell line KPC cells used in animal studies were originated from the KPC mouse model (LSL-*Kras*$^{G12D/+}$;LSL-*Trp53*$^{R172H/+}$;*Pdx1*-Cre), and were a generous donation from Prof. Raghu Kalluri's lab at MD Anderson Cancer Center (Houston, TX, USA). KPC cells were cultured in McCoy's 5A Modified Medium (Thermo Fisher Scientific, Waltham, MA, USA) with 10% fetal bovine serum (FBS; Thermo Fisher Scientific) and 1% penicillin-streptomycin (Genom, Hangzhou, Zhejiang, China). The murine pancreatic ductal carcinoma cell line PANC02, human pancreatic ductal carcinoma cell lines SW1990 and BxPC-3, and human embryonic kidney cell line 293T were obtained from the American Type Culture Collection (Manassas, VA, USA), which were cultured in high-glucose Dulbecco's modified Eagle's medium (DMEM) (Gibco, Grand Island, NY, USA) enriched with 10% FBS and 1% penicillin-streptomycin. All cell lines were incubated at 37°C with 5% $CO_2$ in a humidified incubator. All cell lines used in this study were tested to confirm that they were free of mycoplasma and authenticated by short tandem repeat analysis.

### 2.2 | Human tissues, serum, and clinical information

Human tissues, serum samples, and clinical data were collected from the Department of Hepatobiliary and Pancreatic Surgery at the First Affiliated Hospital, School of Medicine, Zhejiang University (Hangzhou, Zhejiang, China). Wuhan Servicebio Technology (Wuhan, Hubei, China) created paraffin-embedded PDAC tissue arrays comprising samples from 148 patients. The protocol was approved by the Institutional Review Board at First Affiliated Hospital, School of Medicine, Zhejiang University (Approval No. 2024-726), and written informed consent was obtained from all patients at the time of enrollment.

The present study evaluated the efficacy and safety of PD-1 inhibitor therapy in patients with PDAC using data from a clinical trial (NCT03977272). Within three days prior to anti-PD-1 therapy, PDAC patients were tested for liver function, kidney function, blood glucose, blood lipids, urine and blood electrolytes. Blood biochemistry indexes were detected using an automatic biochemical analyzer (VITROS 5600, Johnson, New Brunswick, NJ, USA). According to the Response Evaluation Criteria in Solid Tumors version 1.1 (RECIST), patients with objective response included complete and partial response patients; patients with non-objective response included stable disease and progressive disease patients. The primary endpoint was overall survival (OS), calculated from the date of randomization until the patient's death or the end of the follow-up period, whichever occurred first. Inclusion and exclusion criteria, intervention measures, study outcomes, and follow-up procedures were reported in details [19].

### 2.3 | Mice strains

Male 6- to 8-week-old C57BL/6 mice and BALB/c nude mice were purchased from the Model Animal Research Center of Nanjing University (Nanjing, Jiangsu, China), female 6-week-old human-PBMC NCG mice were pur-

chased from GemPharmatech (Nanjing, Jiangsu, China), and housed in specific pathogen-free (SPF) conditions in cages of up to five animals. The *Tgfb*$^{Rfl/+}$ mice and *Ptfla*-cre mice were purchased from the Jackson Laboratory (Bar Harbor, ME, USA); LSL-*Kras*$^{G12D}$ mice, LSL-*Trp53*$^{R172H/+}$ mice and *Pdx1*-Cre mice were a kind gift from Prof. Raghu Kalluri's lab at MD Anderson Cancer Center (Houston, TX, USA). The aforementioned five types of mice were crossbred. Primers were constructed, and genotyping was performed on the offspring of the crossbred mice to select for KPC or KTC. Male 6- to 8-week-old OT1 mice were purchased from the Cyagen Bioscience (Suzhou, Jiangsu, China). All mice were maintained under a 12-h dark/12-h light cycle with food and water provided ad libitum.

## 2.4 | Mouse models

Subcutaneous/orthotopic xenograft models: KPC cells ($7 \times 10^5$ cells per mouse) and PANC02 cells ($3 \times 10^5$ cells per mouse) were collected by centrifugation (600 rpm, 20°C, 5 min) and suspended in 100 μL of serum-free medium for the subcutaneous injection model or 25 μL of a mixture containing 10 μL Matrigel (356234, Corning Inc., Corning, NY, USA) plus 15 μL serum-free medium for the orthotopic injection model. For the subcutaneous injection model, cell suspension were injected into the right flanks of C57BL/6 and BALB/c nude mice. Tumor growth was measured every three days using calipers, with volume calculated as $0.5 \times \text{length} \times \text{width}^2$. For orthotopic models, cell suspension were injected into the pancreas of C57BL/6 and BALB/c nude mice, and mice were sacrificed after three weeks for tumor weight measurement and subsequent experiments. The following mouse experiments were modeled according to this method.

Survival experiments: KPC cells ($1 \times 10^6$ per mouse) or PANC02 cells ($3 \times 10^5$ cells per mouse) in 25 μL serum-free medium and injected into the pancreas. Mouse survival was tracked, and a survival curve was plotted.

Lipid metabolism inhibitors therapies: KPC cell tumor models were treated with lipid metabolism inhibitors (TVB-2640, Lovastatin, Simvastatin, and Fatostatin) and PD-1 mAb [17]. A week post-tumor implantation, the mice were divided into six groups: Vehicle + IgG2a (BE0089, BioXCell, West Lebanon, NH, USA) (150 μg per mouse; intraperitoneal injection; every 3 days), Vehicle + PD-1 mAb (BE0273, BioXCell) (150 μg per mouse; intraperitoneal injection; every 3 days), PD-1 mAb + TVB-2640 (HY-112829, MedChemExpress, New Brunswick, NJ, USA) (10 mg/kg; intragastric administration; every day), PD-1 mAb + Lovastatin (HY-N0504, MedChemExpress) (10 mg/kg; intragastric administration; every day), PD-1 mAb + Simvastatin (HY-17502, MedChemExpress) (50 mg/kg; intragastric administration; every day), PD-1 mAb + Fatostatin (S8284, Selleck, Houston, TX, USA) (30 mg/kg; intragastric administration; every day). Two weeks after treatment, the mice were euthanized by cervical dislocation, and both body and tumor weights were measured. The following mouse experiments utilized the same reagents, with identical methods of application and dosages. Additionally, the timing for euthanasia and tumor collection procedures were consistent across all experiments.

High-fat diet (HFD) mouse model: Mice were fed a 60% fat diet (D12492, Research Diets, New Brunswick, NJ, USA) for 4 weeks, starting from 4 weeks of age. The control group received a standard chow diet (CD) (7912, Teklad, Madison, WI, USA). Both HFD and control mice were orthotopically implanted with KPC cells, and the mice were divided into two groups: Vehicle + IgG2a and Fatostatin + PD-1 mAb.

Combination therapies: Orthotopic KPC/PANC02 models were treated with combinations of Fatostatin, PD-1 mAb, cytotoxic T-lymphocyte associated protein 4 (CTLA4) mAb (BE0131, BioXCell) (150 μg per mouse; intraperitoneal injection; every 3 days), gemcitabine (GEM, S1149, Sellcek) (10 mg/kg; intraperitoneal injection; every 2 days), Evolocumab (Amgen, Thousand Oaks, CA, USA) (400 μg per mouse; intraperitoneal injection; every 3 days), and Alirocumab (Regeneron, Tarrytown, NY, USA) (400 μg per mouse; intraperitoneal injection; every 3 days). The mice were divided into different groups and subjected to corresponding treatments, with specific details provided in the figures.

KPC re-challenge model: Subcutaneous KPC models were evenly divided into two groups: Vehicle + IgG2a, Fatostatin + PD-1 mAb. Monitor the tumor growth curves. At two weeks, mice were anesthetized, tumors were carefully removed and incisions were sewn up. Mice were then put back in their cages. No new tumors were felt 100 days after the first implant. Then, KPC cells ($2 \times 10^6$ /100 μL) were injected into the other side of the mice. Control mice of the same age, untreated, were injected with KPC cells ($2 \times 10^6$ /100 μL) into their left flanks, and their tumor growth was tracked.

PDX-huPBMC model: Fresh PDAC tumor pieces were implanted under the skin of sedated female BALB/c nude mice using a spinal needle. Mice were kept in a sterile, SPF environment for up to 3 months. PDX tumors were routinely transferred when they reached 1 $cm^3$. Small PDAC tumor pieces (tumor volume = 1 $mm^3$) from PDX were implanted into sedated huPBMC NCG mice. About two weeks later, the mice were divided into four groups: Ctrl, Evolocumab (200 μg per mouse; intraperitoneal injection, every 7 days), Pembrolizumab (PD-1 neutralizing antibody; HY-P9902, MedChemExpress) (100 μg per mouse; intraperitoneal injection every 7 days), and Evolocumab + Pembrolizumab.

$CD8^+$ T cells depletion: Mice received intraperitoneal injections of 200 μg CD8α mAb (BE0004-1, BioXcell) or isotype control (IgG2a) at 3 days before orthotopic inoculation with KPC tumor cells. CD8α mAb was given every three days throughout the study. To detect the clearance efficiency of $CD8^+$ T cells, the proportion of $CD8^+$ T cells in the spleen was measured by flow cytometry.

GEMM-KTC model (LSL-$Kras^{G12D/+}$;$Tgfb^{Rfl/+}$;*Ptfla*-cre driven spontaneous PDAC): $Kras^{G12D/+}$ mice were crossed with $Tgfb^{Rfl/+}$ mice to produce double heterozygotes, which were then crossed with *Ptfla*-cre mice. Offspring were genotyped to confirm the mutations. After the mice reached 4 weeks of age, abdominal palpation was performed every 3 days. When the solid tumor was palpable, the treatments were commenced. Tumor-bearing mice were evenly divided into four groups: Ctrl + IgG2a, Evolocumab + IgG2a, Ctrl + PD-1 mAb, Evolocumab + PD-1 mAb. The drug was administered every three days, and mouse survival was recorded.

Specimen collection and preservation: The tumors obtained from the aforementioned experiments were partially preserved in formalin for IHC and partially stored at -4°C for subsequent studies. Before euthanasia, mouse blood was collected via retro-orbital bleeding, clotted at room temperature for 2 hours, and centrifuged at 2000 rpm for 5 minutes to obtain serum. Serum was analyzed for lipid profiles, electrolytes, and liver/kidney function markers.

Details of the administration of inhibitors and antibodies are provided in Supplementary Table S1. The animal experiments were conducted in strict accordance with the ethical standards set by the Ethics Committee of the First Affiliated Hospital, School of Medicine, Zhejiang University. Animals were monitored daily for signs of distress, including weight loss, lethargy, or tumor burden. The humane endpoint was defined as a 20% weight loss or severe lethargy. Cervical dislocation was performed using euthanasia to ensure a quick and painless death.

## 2.5 | 5 siRNA, plasmids and vectors

For the stable transfection cell lines, sterol regulatory element-binding transcription factor 1 (*SREBF1*) and *PCSK9* short hairpin RNA (shRNA) lentiviral vectors were purchased from Obio Tech (Shanghai, China) and Tsingke Biotechnology (Beijing, China). Human and mouse Flag-*SREBF1* overexpression (OE), Flag-*CD274*-OE were synthesized by Obio Tech. Human and mouse His-*Pcsk9*-OE were synthesized by Miaoling biology (Wuhan, Hubei, China). For the transient transfection, human signal transducer and activator of transcription (*STAT3*)-OE, hypoxia inducible factor-1 (*HIF-1*)-OE and nuclear factor kappa-B (*NF-κB*)-OE were purchased from SinoBiological (Beijing, China). *PCSK9* small interfering RNAs (siRNAs) were synthesized by Guangzhou RiboBio (Guangzhou, Guangdong, China). CRISPR single guide RNAs (sgRNAs) targeting *SREBF1*, *CD274*, Fatty acid synthase (*FASN*), Acetyl-CoA carboxylase alpha (*ACACA*), Stearoyl-CoA desaturase 1 (*SCD1*), and *PCSK9* and vectors were purchased from Santa Cruz Biotechnology (Dallas, TA, USA) and Miaoling Biology. Detailed sequences of the inserts are provided in Supplementary Table S2.

## 2.6 | Cell transfections and production of stable cell lines

For transient transfection, cells at 80% confluence were treated with jetPRIME® (Polyplus, Strasbourg, Grand Est, France) in DMEM following the protocol. The plasmids (human and mouse Flag-*SREBF1*-OE, Flag-*CD274*-OE, His-*PCSK9*-OE, *STAT3*-OE, *HIF-1*-OE and *NF-κB*-OE), siRNA (si*PCSK9*), sgRNA (sg*SREBF1*, sg*CD274*, sg*FASN*, sg*ACACA*, sg*SCD1*, sg*PCSK9*) and vehicle were individually co-transfected into PDAC cell lines (KPC and SW1990). After 48 h, cells were split and selected with puromycin (1 mg/mL, InvivoGen, San Diego, CA, USA) for three days. For lentivirus package, human *CD274* and *PCSK9*, mouse *Cd274* and *Pcsk9*, and control empty vectors were individually co-transfected into 293T cells along with the lentiviral packaging plasmids pMD2.G and pxPAX2 (Testobio-Tech, Ningbo, Zhejiang, China) to generate lentiviral particles. Polybrene (5 μg/mL, C0351, Beyotime, Shanghai, China) was added to boost lentiviral particles infection efficiency. After 24 h, medium was replaced with fresh medium, and cells were selected with puromycin. Efficiency of cell transfection was checked by Western blotting and quantitative reverse transcription polymerase chain reaction (qRT-PCR).

## 2.7 | Chromatin immunoprecipitation assay (ChIP)

A ChIP assay was conducted on BxPC-3, SW1990, KPC, and PANC02 cell lysates using ChIP assay kit (P2080S, Beyotime) according to the manufacturer's instruction. Anti-SREBP1 antibodies (sc-13551X) from Santa Cruz Biotechnology were used. DNA was purified with DNA Purification Kit (D0033, Beyotime). JASPAR (http://jaspar.genereg.net) was used to predict *SREBF1*-binding sites to the PD-L1 and PCSK9 promoters, starting 2,000 base pairs upstream. The sequences were aligned for complementarity, and results were confirmed by qRT-PCR. Primers were made by Sunya Biotech (Hangzhou, Zhejiang, China) (Supplementary Table S2).

## 2.8 | Dual luciferase reporter assay

293T cells ($0.5 \times 10^5$ in 200 μL per well) plated in a 96-well plate were co-transfected with 0.1 μg of the expression plasmids (cytomegalovirus [CMV]-flag-*SREBF1* and empty vector), 0.1 μg of the promoter reporter plasmids (pGL4.10 empty vector, pGL4.10-*CD274/ PCSK9* promoter [WT], pGL4.10-*CD274/ PCSK9* promoter [MUT]), and 0.005 μg of the Renilla pRL-CMV (Renilla luciferase) plasmids using jetPRIME®. At 24 h after transfection, the cells were washed and the medium was replaced with fresh medium. The Dual-luciferase reporter assay (Beyotime) was performed after 48 h and the luciferase activity was normalized to the Renilla luciferase activity.

## 2.9 | 9qRT-PCR analysis

Total RNA was extracted using MolPure® Cell/Tissue Total RNA Kit (Yeasen Biotechnology, Shanghai, China) and reverse-transcribed into cDNA using a cDNA synthesis kit (RR047A, Takara, Beijing, China). Quantitative RT-PCR analysis was conducted using the cDNA as the template in a 10 μL reaction system (0.3 μL forward primer, 0.3 μL reverse primer, 5 μL TB Green Premix Ex Taq™ II, 2 μL cDNA diluted 10 times, 2.4 μL RNase-free dd$H_2O$) using a real-time PCR System (7500, Applied Biosystems, Foster City, CA, USA) with TB Green Premix Ex Taq™ II (RR820A, Takara). Thermal cycling conditions consisted of an initial denaturation step at 95°C for 30 s, followed by 40 cycles of denaturation at 95°C for 10 s, annealing at 60°C for 30 s, and extension at 95°C for 15 s. The specific primers used for qRT-PCR are listed in Supplementary Table S2. Samples were analyzed in triplicate. $\beta$-actin was used as an internal reference, and the data were analyzed using the $2^{-\Delta\Delta CT}$ method. The relative gene expression was normalized to that of *GAPDH* (encoding glyceraldehyde-3-phosphate dehydrogenase) or *ACTB* (encoding $\beta$-actin) and calculated using the standard $2^{-\Delta\Delta Ct}$ method [20].

## 2.10 | Western blotting analysis

Cells were lysed using radioimmunoprecipitation assay (RIPA) lysis buffer (P0013B, Beyotime) containing phenylmethanesulfonyl fluoride (ST505, Beyotime) for 30 min on ice, followed by centrifugation at 12,000 × *g*, 4°C for 15 min. The supernatant with proteins was collected and protein concentration was measured using the bicinchoninic acid (BCA) reagent (P0012, Beyotime). Lysates were heated at 100°C, separated by SDS-PAGE (4×) (Thermo Fisher Scientific) for 3-5 min, and transferred to a polyvinylidene fluoride (PVDF) membrane (Millipore, Billerica, MA, USA). Membranes were blocked in 5% milk, incubated with primary antibodies (SREBP1, PD-L1, PCSK9, major histocompatibility complex class I (MHC-I), Vinculin, $\alpha$-Tubulin, lysosome-associated membrane protein 2 (LAMP2), Na/K-ATPase, FASN) overnight at 4°C, then with secondary antibodies at 4°C for 3 h (Supplementary Table S3), and finally the protein bands were visualized.

## 2.11 | Histology and immunohistochemistry analysis (IHC)

PDAC tissues from patients and mouse models were fixed using 10% neutral buffered formalin, embedded in paraffin, and cut into 4-μm slices. Slides were incubated with primary antibodies (Supplementary Table S3) at 4°C overnight, and then with HRP-conjugated secondary antibodies at 37°C for 1 hour. Sirius red staining was performed using a Picrosirius Red Staining Kit (24901, Polysciences, Warrington, PA, USA) according to the manufacturer's instructions. We can clearly tell the lipid droplet under the light microscope after the PDAC tumor (Cryo-section) was stained with Oil Red-staining (ab150678, Abcam, Cambridge, UK). Each slide was assessed in five high-power fields (×100) using the Vectra imaging system (Perkin Elmer, Waltham, MA, USA). GraphPad Prism 9 (GraphPad Software, San Diego, CA, USA) was used to quantify the IHC staining. Wuhan Servicebio technology performed the IHC staining of the tissue array. The IHC results were quantified by processing the images using 3D HISTECH quant center 2.1 software (3D HISTECH, Budapest, Hungary). H-score was calculated as H-score = $\sum$(pi × i), where pi indicates the percentage of cells exhibiting a particular staining intensity (expressed as a decimal, e.g., 20% = 0.20) and i indicates the intensity score assigned to the staining (typically on a scale of 0 to 3, 0 = no staining; 1 = weak staining; 2 = moderate staining; 3 = strong staining). The H-score ranges between 0 and 300, with higher values indicating stronger overall positivity. The median H-score was chosen as the cutoff value for the classification of high and low expression of the protein [21].

## 2.12 | Multiplex immunohistochemistry (mIHC)

To reveal the correlation between the expression of SREBP1, PD-L1, and PCSK9 in pancreatic cancer tumors (markerd by pan-cytokeratin [Pan-CK]) and $CD8^+$ T cells (marked by CD8$\alpha$), multiplex IHC was performed. We utilized the Opal PolarisTM 7-color Manual IHC Kit (NEL861001KT, Akoya, Boston, MA, USA) following the protocol provided by the manufacturer. The opal-stained

slides were then imaged using the Vectra Polaris Quantitative Pathology Imaging Systems (Akoya), after which 2-(4-amidinophenyl)-6-indolecarbamidine dihydrochloride (DAPI) (C1002, Beyotime) staining was applied.

## 2.13 | Immunofluorescence analysis (IF)

Tumor cells were grown in 12-well plates to 70%-80% confluence, then fixed with 4% paraformaldehyde for 15 min at room temperature. After permeabilizing with 0.1% Triton X-100 for 15 min and blocked with 2% BSA for 30 min, cells were incubated with primary antibodies (Supplementary Table S3) overnight at 4°C. They were then washed and incubated with Alexa Fluor555-conjugated anti-mouse IgG (4408, 1:400 dilution, Cell Signaling Technology, Danvers, MA, USA) for 1 hour. Nuclei were stained with DAPI, and visualized under a confocal microscope (TCS SP8 CARS, Leica, Wetzlar, Hesse, Germany).

In experiments to assess lysosomal co-localization, PCSK9 overexpression or PCSK9 knockdown SW1990 cells were stained with Lyso-Tracker Deep Red (L12492, Thermo Fisher Scientific) at 37°C for 20 min, followed by two washes with phosphate-buffered saline (PBS, Beyotime). Subsequently, the cells were incubated with 5 μg/mL CF488 wheat germ agglutinin (GTX01502, GeneTex, Irvine, CA, USA) at 37°C for 10 min to label the cell membrane. After being washed with PBS, cells were fixed using 4% paraformaldehyde for 15 min at room temperature and permeabilized with a blocking buffer containing 1% BSA, 5% donkey serum, and 0.1% digitonin for 30 min at room temperature. They were then incubated with a primary antibody overnight at 4°C, followed by incubation with fluorescently labeled secondary antibodies for 1 h at room temperature. The cells were washed again with PBS, and nuclei were counterstained with 0.02 μg/mL DAPI for 2 min. Cells were visualized using a confocal laser scanning microscope.

## 2.14 | Enzyme-linked immunosorbent assay (ELISA)

The concentration of PCSK9 in the supernatants of PCSK9-knockdown PDAC cells cultures was detected using a mouse PCSK9 ELISA kit (KE10050; Proteintech, Rosemont, PA, USA) according to the manufacturer's instructions. Supernatants were collected after culturing KPC and PANC02 cells in vitro for 48 h. The PCSK9 concentration was normalized by the volume and cell number. The same method was used to detect PCSK9 secreted by SW1990 and BxPC-3 cells cultured in vitro for 48 h using a human PCSK9 ELISA kit (KE00278; Proteintech) according to the manufacturer's instructions. The levels of secreted PCSK9 in patient serum were also measured using this human PCSK9 ELISA kit.

## 2.15 | Flow cytometry analysis

Tumor cells and immune cells from mouse tumors and spleens were isolated for flow cytometry analysis. Tumor tissues were cut into tiny pieces and put into a mix of DMEM (containing 2% FBS), collagenase IV (1 mg/mL, 17104019, Thermo Fisher Scientific), DNase (10 μg/mL, D5025, Sigma-Aldrich, St. Louis, MO, USA), Dispase (0.6 mg/mL, 17105041, Gibco), and $CaCl_2$ (3 mmol/L, 21115, Sigma-Aldrich). These were kept at 37°C and shaken at 200 rpm for 30 to 50 min to break down the tissue. The digestion process was halted by adding DMEM with 10% FBS. The separated tissues were pushed through a 70 μm cell strainer (CLS431751-50EA, Sigma-Aldrich) and rinsed with PBS. Three-quarters of the cells were resuspended in a Percoll mixture (36% Percoll, 4% 10× PBS, 60% serum-free DMEM) and subjected to density gradient centrifugation (500 ×g, accelerate at a rate of 8 and decelerate at a rate of 1, 15 min, 25°C) to remove non-immune cells. These cells were later activated with a Leukocyte Activation Cocktail (550583, BD Biosciences, San Jose, CA, USA), incubated at 37°C for 4-6 h, and stained using a LIVE/DEAD Fixable Violet Dead Cell Stain Kit in the dark on ice to identify dead cells. Next, cells were washed with PBS and blocked using TruStain FcX™ (anti-mouse CD16/32, 156603, Biolegend, San Diego, CA, USA) antibody and stained for cell surface CD45, CD3, CD4, CD8, and CD25 using corresponding antibodies (1:100 dilution, stain in the dark for 30 min). Cells were washed with PBS and fixed and permeabilized using an eBioscience™ Foxp3/Transcription Factor Staining Buffer Set (00-5523-00, Thermo Fisher Scientific). Intracellular staining was performed for Granzyme B (GZMB), Perforin, Tumor Necrosis Factor-alpha (TNF-$\alpha$), Interferon-gamma (IFN-$\gamma$), and Forkhead Box P3 (Foxp3) using corresponding antibodies (1:100 dilution, stain in the dark for 30 min). The other quarter of the tumor cells were also stained using the LIVE/DEAD Fixable Violet Dead Cell Stain Kit to separate live and dead cells, and blocked using TruStain FcX™ (anti-mouse CD16/32) antibody. Next, the cells were stained for CD326 (EpCAM) to identify tumor cells and for PD-L1 to identify surface PD-L1 expression. Spleens were mechanically ground using a grinding rod and washed in PBS. Then, red blood cells were removed by 1× lysis buffer (555899, BD Biosciences). Single-immune cells were also stained with the LIVE/DEAD Fixable Violet Dead Cell Stain Kit to separate live and dead cells, and blocked using TruStain FcX™ (anti-mouse CD16/32) antibodies. Next, cells were stained

for CD45, CD3, and CD8 to identify $CD8^+$ T cells. All samples were analyzed using flow cytometry on a BD LSR-Fortessa flow cytometer and the data were analyzed by FlowJo software (TreeStar Inc., Ashland, OR, USA).

## 2.16 | T cell-mediated tumor cell killing assay

$CD8^+$ T cells were isolated from OT1 mice spleens using a $CD8^+$ T Cell Isolation Kit (130-090-859; Miltenyi Biotec, Bergisch Gladbach, North Rhine-Westphalia, Germany), an LS Column, and a MidiMACS™ Separator (130-042-301; Miltenyi Biotec) according to the manufacturer's instructions. $CD8^+$ T cells were stimulated with CD3/CD28 monoclonal antibodies (mAbs) (100 ng/mL, Thermo Scientific) and recombinant Murine interleukin 2 (IL-2) (10 ng/mL, PeproTech, Cranbury, NJ, USA) in RPMI-1640 medium (C11875500BT, Gibco) with 10% FBS and 1% antibiotic for 3 days. Tumor cells transfected with OVA plasmid were allowed to adhere to the plates overnight and then cultured with the activated T cells for 48 h at a ratio of 1:8 to 1:10. T cells and cell debris were removed and washed three times using PBS. The remaining living cancer cells were fixed with 4% paraformaldehyde, stained with 0.5% crystal violet, and OD at 450 nm was quantified using a spectrophotometer.

## 2.17 | Co-immunoprecipitation (Co-IP)

Cells were lysed in IP/Western lysis buffer supplemented with protease and phosphatase inhibitor cocktails for 30-40 min at 4°C, then centrifuged at 12,000 × g 4°C for 15 min to pellet debris. The supernatant was used for immunoprecipitation with specific antibodies, which was incubated for 4-6 h before the addition of Protein A/G PLUS-Agarose and further incubated for 2-4 h at 4°C with gentle agitation (30 rpm). After three washes with a buffer containing 10% IP/Western lysing in PBS, the immunoprecipitated proteins were denatured at 100°C in NuPAGE LDS Sample Buffer (NP007, Thermo Fisher Scientific) for 5-10 min prior to Western blotting analysis as previously described [22].

## 2.18 | Glutathione S-transferase (GST) pull-down assay

Recombinant human GST (ab70456, Abcam), PD-L1-GST (ag12432, Proteintech), and PCSK9-His (Eg0199, Proteintech) proteins were used for a GST pull-down assay. The binding of GST and PD-L1-GST to glutathione beads and the subsequent pull-down assay were carried out using the Pierce GST Protein Interaction Pull-Down Kit (21516, Thermo Fisher Scientific) following the protocol provided by the manufacturer.

## 2.19 | RNA-sequencing (RNA-seq)

RNA was isolated from shNC and shSREBP1 KPC and PANC02 cells ($5\times10^6$ cells, per group, with three replicates) using MolPure® Cell/Tissue Total RNA Kit. The RNA samples underwent quality assessment before proceeding with the analysis. Post-assessment, mRNA was enriched with magnetic oligo (dT) beads to create a sequencing library. Adapter ligation and size selection were then performed, followed by amplification of the cDNA library. Sequencing was performed on the Novaseq 6000 platform (Illumina, San Diego, CA, USA). Library preparation, sequencing, and data processing were accomplished by GENEWIZ (South Plainfield, NJ, USA). Gene expression levels were normalized to fragments per kilobase of exon model per million mapped fragments (FPKM), and differentially expressed genes (DEGs) were identified with a significance threshold of $P < 0.05$ and a $|\log2 (\text{fold change})| > 1$. DEGs were used through the R package clusterProfiler for gene ontology (GO) analysis and gene set enrichment analysis (GSEA), and the results were visualized through the R package ggplot2.

## 2.20 | Non-targeted metabolomics

The metabolic profiles of cells (shNC and shSREBP1 KPC) were analyzed using liquid chromatography (LC) (Dionex U3000 UHPLC, Thermo Fisher)-tandem mass spectrometry (MS) (Q-Exactive, Thermo Fisher). Briefly, shNC and shSREBP1 KPC cells were collected, frozen, and broken up. Samples were processed through a gradient elution system utilizing two mobile phases: Phase A (99.9% water with 0.1% formic acid) and Phase B (99.9% acetonitrile with 0.1% formic acid). The gradient program involved several steps: initially, Phase A was reduced from 100% to 95% over 2 min, then to 70% over the next 2 min, further to 50% over 4 min, to 20% over 2 min, and finally to 0% over 4 min. The system held at 0% Phase A for 1 min before rapidly increasing back to 95% Phase A in 5 s and holding there for 55 s. The elution was performed at a flow rate of 0.35 mL/min, with the column maintained at 45°C and an injection volume of 2 μL. The mass spectrometer collected signals continuously, operating at a capillary temperature of 320°C and a spray voltage of 3,800 V.

To analyze the metabolic changes among the experimental groups, principal component analysis (PCA) and orthogonal partial least-squares discriminant analysis

(OPLS-DA) were employed after applying mean centering and Pareto variance scaling. The Hotelling's $T^2$ ellipse in the score plots indicated the 95% confidence interval for the modeled variations. To ensure the model's reliability, seven-fold cross-validation was used, excluding a seventh of the samples in each iteration to avoid overfitting. Furthermore, 200 response permutation tests were conducted to assess the model's robustness against overfitting. The original model's $R^2Y$ and $Q^2Y$ were used for linear regression analysis, with the Y-intercept values ($R^2$ and $Q^2$) helping to evaluate any potential overfitting of the OPLS-DA model. Variables contributing significantly to the model, identified by a VIP score greater than 1, were deemed important for distinguishing between groups. Metabolite annotation and analysis were facilitated by the Kyoto Encyclopedia of Genes and Genomes (KEGG) database. The classifier's effectiveness across various decision thresholds was assessed by calculating the area under the curve (AUC) area under the receiver operating characteristic curve from the receiver operating characteristic (ROC) curve.

## 2.21 | Mass spectrometry-based proteomics

Human and mouse PDAC tissue samples were collected and homogenized. Proteins were extracted using lysis buffers, and the sample was centrifuged (12,000 × g, 4°C, 15 min)to separate the protein-containing supernatant. The concentration of proteins in the sample was measured using BCA assays. Proteins were denatured, typically with heat or chemical agents, and reduced with agents like dithiothreitol (DTT) to break disulfide bonds. Reduced proteins were alkylated with 5 mmol/L iodoacetamide (IAA, I1149, Sigma-Aldrich) to prevent reformation of disulfides, followed by enzymatic digestion with 5 μg/mL trypsin (V5111, Promega, Madison, WI, USA), to cleave proteins into peptides. Mass spectrometry analysis was carried out by PTM-Biolabs Co., Ltd. (Hangzhou, Zhejiang, China) following established protocols [22].

## 2.22 | Cleavage under targets and tagmentation (CUT & Tag) sequencing

Each cell sample (SW1990 control and SW1990 SREBP1 OE) was prepared using a total of $1 \times 10^5$ cells. Cells were harvested, counted and centrifuged for 3 min at 600 ×g at room temperature. Aliquots of cells (60-500,000 cells) were washed twice in 1.5 mL Wash Buffer (20 mmol/L HEPES pH 7.5; 150 mmol/L NaCl; 0.5 mmol/L Spermidine; 1× Protease inhibitor cocktail) by gentle pipetting. ChIP-grade SREBP1 antibody was purchased from Proteintech (14088-1-AP, 5μg per sample). CUT & Tag data analysis was performed by Novogene (Beijing, China). For sequencing library construction, DNA was PCR amplified using a TruePrep Index Kit V2 (TD202, Vazyme, Nanjing, Jiangsu, China). The experimental protocol was conducted as previously described [23].

## 2.23 | Cell proliferation assay

We measured cell growth by Cell Counting Kit-8 (CCK-8) assay (HY-K0301, MedChemExpress) as previously delineated. Briefly, $1 \times 10^4$ cells (KPC shNC, shSREBP1#1, shSREBP1#2; PANC02 shNC, shSREBP1#1, shSREBP1#2; BxPC-3 shNC, shSREBP1#1, shSREBP1#2; SW1990 shNC, shSREBP1#1, shSREBP1#2) per well were seeded in a 96-well plate, and the plate was incubated in a humidified incubator at 37°C with 5% CO2 for 12, 24, 48 or 72 h. Subsequently, 10 μL of CCK-8 solution was added to each well, and the plate was incubated for 45 min at 37°C. The absorbance at 450 nm was measured using a spectrophotometer.

## 2.24 | Transwell assays

The experimental protocol was conducted as previously described [24]. The migrative capacity of PDAC cells (KPC shNC, shSREBP1#1, shSREBP1#2; PANC02 shNC, shSREBP1#1, shSREBP1#2; BxPC-3 shNC, shSREBP1#1, shSREBP1#2; SW1990 shNC, shSREBP1#1, shSREBP1#2) were assessed using the transwell system (3422, Corning). In brief, $2 \times 10^4$ cells were seeded in the upper chamber with serum-free culture medium, while the lower chamber was filled with 500 μL of complete medium. The cells in the chambers were incubated at 37°C in a 5% $CO_2$ atmosphere. Following incubation, the migrated cells were fixed with 10% formalin and stained with 0.1% crystal violet. The number of migratory cells was quantified using Image-Pro Plus 6.0 image analysis software (Media Cybernetics, Bethesda, MA, USA). Cell invasion assays were conducted using Transwell insert chambers (3413, Corning) pre-coated with Matrigel matrix (1 mg/mL, 356234, Corning). The remaining steps were performed following the same protocol as described for the migration assay.

## 2.25 | Molecular docking analysis

Rigid docking simulations were conducted between SEPT9 and HIF-1α to explore their interactions, utilizing GRAMM-X (http://gramm.compbio.ku.edu/). The struc-

tural domains of PCSK9 (PDB ID: 5ius) and PD-L1 (PDB ID: 7anq) were sourced from the Protein Data Bank (PDB database (http://www.rcsb.org/). Visualization of the docking complex was achieved using PyMOL (version 2.4, Schrödinger, New York, NY, USA) and LigPlus (version 2.2.8, EMBL-EBI, Hinxton, Cambridgeshire, UK), which presented the interactions as a 2D graphic. In these graphics, green dashed lines indicate hydrogen bonds, and spiral arcs denote residues involved in non-covalent interactions with the ligand.

## 2.26 | Cholesterol and PCSK9 inhibition assay

For Cholesterol assay, $5 \times 10^5$ KPC cells per well were seeded in a 6-well plate, and treated with or without Cholesterol (10, 50 and 100 μmol/L, HY-N0322A, MedChemExpress) for 48 h. For PCSK9 inhibition assay, $5 \times 10^5$ KPC, PANC02, SW1990 and BxPC-3 cells per well were seeded in a 6-well plat, and treated with or without PF-06446846 (5 and 10 μmol/L, HY-120088, MedChemExpress) for 48 h. Analysis of PCSK9 and PD-L1 expression in PDAC cell lines was performed by Western blotting.

## 2.27 | Protein stability and degradation assays

KPC sgNC and sgPCSK9 cells were seeded at $5 \times 10^5$ cells per well in 6-well plates and treated with cycloheximide (CHX; 20 μmol/L, 239763-M, Sigma-Aldrich) for 0, 6, 12 and 24 h or bafilomycin-A1 (Baf-A1; 50 nmol/L, HY-100558, MedChemExpress) for 0, 1, 8 and 16 h. PD-L1 expression in KPC cells was detected by Western blotting.

## 2.28 | Fatty acid analysis

KPC cells with SREBP1 knockdown and those treated with Fatostatin were harvested for fatty acid profiling using gas chromatography-mass spectrometry (GC-MS, BIOTREE, Shanghai, China) following the manufacturer's recommended procedures.

## 2.29 | Database analysis

We used the "clusterProfiler" R package for KEGG gene annotation, with a significance level setting at $P < 0.05$. Hallmark gene sets were derived from the Molecular Signatures (MSigDB) database (https://www.gsea-msigdb. org/gsea/index.jsp). The "TCGAbiolinks" R package (Version 2.14.1) was used to retrieve level-3 RNA-seq data across 23 types of cancers from The Cancer Genome Atlas Network (TCGA, GDC v16.0). GSEA was conducted using MSigDB. Tumor-immune interactions were analyzed using the Tumor Immune Estimation Resource (TIMER, https://cistrome.shinyapps.io/timer) and GEPIA2 (http://gepia2.cancer-pku.cn).

## 2.30 | Statistical analyses

Statistics were calculated with SPSS (version 20) and GraphPad Prism (version 7.0). Results from at least three experiments are shown as average ± standard deviation (SD), while clinical information as median interquartile range (IQR). We used *t*-tests or Mann-Whitney *U* tests to see differences between two groups. For three or more groups, we did a one-way analysis of variance (ANOVA). To examine the relationships between variables, we used

**TABLE 1** Univariate analyses of serum lipid and blood glucose levels in 43 PDAC patients received anti-PD-1 therapy

| Variable | Objective response group ($n = 20$) | Non-objective response group ($n = 23$) | *P* value |
|---|---|---|---|
| Age, years, median (IQR) | 65 (57-72) | 63 (57-67) | 0.542 |
| Sex, *n* (%) | | | 0.637 |
| Male | 16 (48.5%) | 17 (51.5%) | |
| Female | 4 (40.0%) | 6 (60.0%) | |
| BMI, median (IQR) | 22.25 (20.20-24.13) | 21.50 (20.20-24.60) | 0.808 |
| TC, mmol/L, median (IQR) | 3.33 (2.99-3.57) | 4.09 (3.63-4.71) | **0.001** |
| HDL-C, mmol/L, median (IQR) | 0.87 (0.72-1.26) | 1.16 (0.94-1.35) | **0.007** |
| LDL-C, mmol/L, median (IQR) | 1.89 (1.66-2.23) | 2.38 (1.81-2.89) | **0.043** |
| TG, mmol/L, median (IQR) | 1.01 (0.77-1.54) | 1.18 (0.81-1.45) | 0.836 |
| FBG, mmol/L, median (IQR) | 5.64 (5.19-6.51) | 5.83 (5.11-6.83) | 0.480 |

Abbreviations: PDAC, pancreatic ductal adenocarcinoma; PD-1, programmed death 1; IQR, interquartile range; BMI, body mass index; TC, total cholesterol; HDL-C, high-density lipoprotein-cholesterol; LDL-C, low-density lipoprotein-cholesterol; TG, triglyceride; FBG, fasting blood glucose.

Spearman's rank correlation. Tumor growth was assessed with *t*-tests. Survival rates were figured out with the Kaplan-Meier method and the Gehan-Breslow-Wilcoxon test. A *P* value under 0.05 meant it was significant.

## 3 | RESULTS

### 3.1 | Targeting SREBP1 disrupted lipid metabolism and immunosuppressive TME, sensitizing PDAC tumors to immunochemotherapy

We evaluated the prognostic value of serum lipids and blood glucose in PDAC patients from the NCT03977272 trial who were treated with anti-PD-1 therapy [19]. Peripheral blood samples for analysis were collected before the initiation of anti-PD-1 therapy. Our results indicated that patients with an objective response to anti-PD-1 therapy had lower serum lipids than those with a non-objective response (Table 1). Using a median total cholesterol (TC) level of 3.6 mmol/L as the cutoff for the cohort of 43 patients, we found that patients with low serum TC levels had longer OS compared to those with higher serum TC levels (Figure 1A). We hypothesized that inhibiting lipid metabolism could enhance the sensitivity to anti-PD-1 therapy in PDAC patients. To test this, we applied four lipid metabolism inhibitors (TVB-2640, Lovastatin, Simvastatin, and Fatostatin) to KPC cell mouse models (Supplementary Figure S1A). Fatostatin, a SREBP-specific inhibitor, in combination with PD-1 mAb exerted optimal antitumor activity (Supplementary Figure S1B), and Fatostatin sensitized PDAC tumor to PD-1 mAb therapy (Figure 1B-D). At the end of the treatment period, there was no significant difference in body weight between the vehicle, Fatostatin, PD-1 mAb and Fatostatin + PD-1 mAb groups (Supplementary Figure S1C), and tumor samples were harvested for further analysis. Flow cytometry and IHC staining analysis showed that the combination therapy significantly increased the tumor-infiltrating cytotoxic $CD8^+$ T cell population in mice (Figure 1E-F). We repeated the treatment experiments in the orthotopic PANC02 cell tumor model and obtained results consistent with the KPC cell tumor model (Supplementary Figure S1D-G). These results indicated that the combination of Fatostatin and PD-1 mAb significantly increased cytotoxic T cell infiltration and enhanced the antitumor effects of ICB therapy.

To further test whether $CD8^+$ T cells are essential for the joint effect of combination treatment with PD-1 mAb and Fatostatin, we conducted in vivo experiments using CD8α mAb (Figure 1G). We observed that the combined effect was substantially abrogated by cotreatment with CD8α mAb in KPC PDAC mouse models (Figure 1H and Supplementary Figure S1H-I). Therefore, our results suggested that $CD8^+$ T cells were required for the joint effect of PD-1 mAb and Fatostatin combination treatment. Similar to the treatment with PD-1 mAb for PDAC, we observed that cotreatment with CTLA4 mAb and Fatostatin in mice also significantly decreased the tumor weight compared to the other groups (Supplementary Figure S1J-K).

Endo et al. [25] demonstrated that fatty acid metabolism directs cell fate determination during the generation of memory $CD4^+$ T cells. To determine whether immunological memory is induced by combination therapy with Fatostatin and PD-1 mAb, tumor-free mice from the initial subcutaneous models—produced by removal of the subcutaneous tumors—were challenged by implantation of syngeneic PDAC cells from either the same cell line as the first implantation or a different cell line, with age-matched wild-type mice serving as controls. No additional therapy was provided to the rechallenged mice (Supplementary Figure S1L). The KPC rechallenge model showed that combined treatment with Fatostatin and anti-PD-1 resulted in both immediate antitumor activity and long-term immune memory (Supplementary Figure S1M-N).

Compared with vehicle controls, Fatostatin increased cancer cell apoptosis and reduced the cancer cell proliferation, collagen deposition, and activity of cancer-associated fibroblast (CAF) (Supplementary Figure S2A-B). These findings suggested that Fatostatin may enhance PDAC responsiveness to chemotherapy. To more closely align with clinical treatment protocols, Fatostatin was administered in combination with GEM and/or PD-1 mAb (Supplementary Figure S2C). As anticipated, the addition of Fatostatin increased responsiveness to GEM or to GEM combined with PD-1 mAb, thereby enhancing the susceptibility of PDAC to chemotherapy or immunotherapy (Supplementary Figure S2D-E). Given that targeting SREBP1 disrupts the desmoplastic and immunosuppressive TME in PDAC, we hypothesized that the combined effects would be particularly pronounced in a cohort of tumor-bearing mice where Fatostatin treatment was initiated 3 days prior to PD-1 mAb administration. This hypothesis was indeed validated through in vivo experiments in mice (Supplementary Figure S2F-G).

Oil red O staining confirmed that Fatostatin treatment significantly reduced lipid droplet formation in the tumor region (Figure 1I). Proteomics analysis was conducted to compare proteins in isolated tumors from the control and Fatostatin-treated groups (Supplementary Figure S3A), aiming to explore the specific mechanism of which Fatostatin sensitizes PDAC to immunochemotherapy. KEGG enrichment analysis showed downregulation of the fatty acid metabolism and synthesis pathways, but not cholesterol metabolism, in Fatostatin-treated tumors (Figure 1J). SREBP1-related proteins FASN, ACACA, acyl-

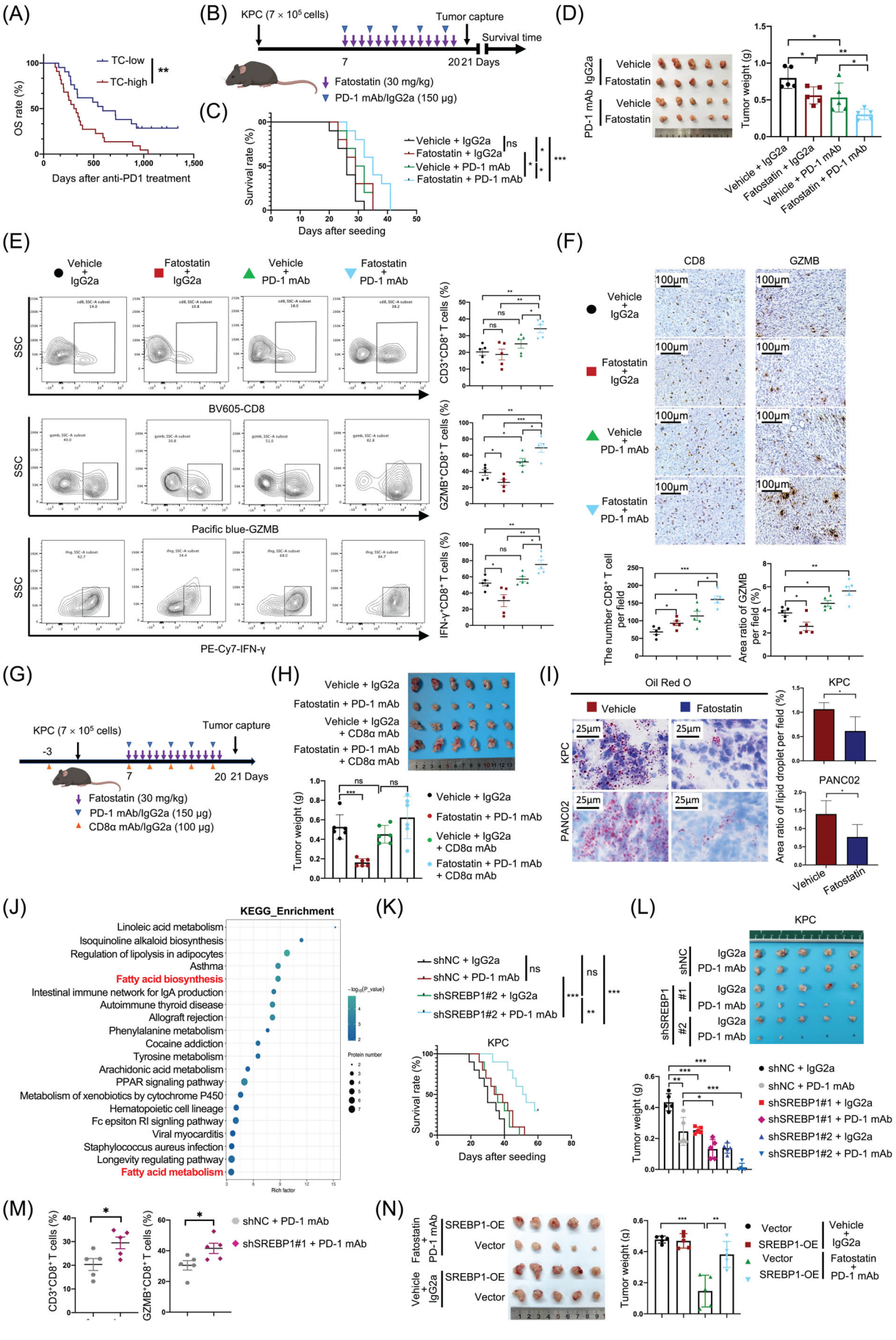

CoA synthetase long-chain family member 1 (ACSL1), microsomal glutathione S-transferase 1 (MGST1), and fatty acid-binding protein 4 (FABP4) were downregulated by at least 2-fold in Fatostatin-treated tumors (Supplementary Figure S3B). In addition, serum biochemical markers were assessed in both the control and Fatostatin-treated groups. In the Fatostatin-treated group, serum levels of TC and high-density lipoprotein-cholesterol (HDL-C) were downregulated (Supplementary Table S4). Next, stable SREBP1-knockdown KPC and PANC02 mouse PDAC cell lines, as well as SW1990 and BxPC-3 human PDAC cell lines, were constructed (Supplementary Figure S3C). We utilized a PD-1 mAb to treat immune-competent mice inoculated with shSREBP1 KPC and PANC02 cells or control cells. We observed that cotreatment with PD-1 mAb and shSREBP1 further decreased the tumor weight and extended animal survival time compared to shSREBP1 or PD-1 mAb treatment alone (Figure 1K-L and Supplementary Figure S3D-E). Compared to PD-1 mAb treatment alone, shSREBP1 plus PD-1 mAb significantly increased tumor-infiltrating cytotoxic $CD8^+$ T cell population (Figure 1M and Supplementary Figure S3F).

Similar to the results from Fatostatin treatment, Oil red O staining and IHC showed that SREBP1 knockdown inhibited lipid droplet formation, cell proliferation, collagen deposition, CAF activation, and increased tumor apoptosis compared to the control group (Supplementary Figure S3G). Ultimately, the ectopic expression of cleaved SREBP1 in KPC cells reversed the effect of PD-1 mAb and Fatostatin combination therapy in mice (Figure 1N). However, simply feeding mice a high-fat diet did not antagonize the antitumor effects of PD-1 mAb and Fatostatin in KPC tumor-bearing mice (Supplementary Figure S3H-I). These data suggest that, in contrast to inhibiting whole-body lipid metabolism, Fatostatin primarily reduced SREBP1-mediated fatty acid metabolism in tumors, thereby suppressing tumor growth and sensitizing PDAC to immunochemotherapy.

## 3.2 | SREBP1 overexpresstion aggravated the immunosuppressive TME and reprogramming of lipid metabolism in PDAC

We compared lipid droplet levels between cancer tissues and adjacent normal tissues from patients with PDAC using Oil Red O staining. The results showed more dispersed lipid vacuoles in human PDAC specimens than in matched adjacent non-tumor tissues (Figure 2A). Similarly, compared to normal mouse pancreas tissues, Oil Red O staining showed a higher level of lipid droplets in KPC (LSL-*Kras*$^{G12D/+}$;LSL-*Trp53*$^{R172H/+}$;*Pdx1*-Cre) and KTC (LSL-*Kras*$^{G12D/+}$;*Tgfb*$^{Rfl/+}$;*Ptfla*-cre) tumor tissues (Figure 2B). In an analysis of protein expression differences between cancer tissues and adjacent normal tissues sampled from 5 PDAC patients, we observed a marked upregulation of proteins associated with fatty acid metabolism and pronounced activation of the SREBPs signaling pathway in cancer tissues (Figure 2C-D). IHC results demonstrated elevated levels of SREBP1 in KPC and KTC tumor tissues compared to normal mouse pancreas tissues (Figure 2E). In PDAC patient tissues and the TCGA database, PDAC tissues exhibited higher SREBP1 expression compared to paired normal tissues (Figure 2F-H). Furthermore, SREBP1 was primarily overexpressed in cancer cells, not CAFs (marked by $\alpha$-SMA) (Figure 2I-J). SREBP1 expression was positively correlated with the lipid droplet volume, as analyzed tumor tissues from 29 PDAC patients (Figure 2K-L). Moreover, SREBP1-deficient KPC

**FIGURE 1** Combined effect of PD-1 mAb and Fatostatin combination treatment is dependent on $CD8^+$ T cells and SREBP1-deficiency of cancer cells. (A) Overall survival of the PDAC patients following Sintilimab therapy stratified by median serum TC levels ($n = 43$). (B-F) C57BL/6 mice were implanted with $7 \times 10^5$ KPC cells and co-treated with Fatastatin and PD-1 mAb. (B) A schematic view of the treatment plan. (C) Kaplan-Meier survival curves for each group (10 mice/group). (D) Tumor image and statistical analysis of orthotopic PDAC model (5 mice/group). (E-F) Representative images and statistical results of tumor-infiltrating lymphocytes ($CD8^+$ T cells, $GZMB^+CD8^+$ T cells, and IFN-$\gamma^+CD8^+$ T cells) are shown as indicated by flow cytometry (E) and IHC (F). (G-I) C57BL/6 mice were implanted with $7 \times 10^5$ KPC cells and received Fatostatin, PD-1 mAb, CD8$\alpha$ mAb or IgG isotype control (IgG2a) treatment. (G) A schematic view of the treatment plan. (H) Tumor image and statistical analysis of orthotopic PDAC model (6 mice/group). (I) Oil Red O staining was treated with Fatostatin or vehicle control in C57BL/6 mice xenograft tumor samples. (J) KEGG enrichment analysis of proteomics in KPC tumor treated with Fatostatin or vehicle control. (K-M) C57BL/6 mice were implanted with $7 \times 10^5$ shSREBP1 KPC or shNC cells and received PD-1 mAb or IgG2a treatment. (K) Kaplan-Meier survival curves for each group (10 mice/group). (L) Tumor image and statistical analysis of orthotopic PDAC model (5 mice/group). (M) Statistical results of tumor-infiltrating lymphocytes ($CD8^+$ T cells, $GZMB^+CD8^+$ T cells) are shown as indicated by flow cytometry. (N) Tumor image and statistical analysis of C57BL/6 mice implanted with $7 \times 10^5$ SREBP1-OE or Vector KPC cells and treated Fatostatin plus PD-1 mAb. Results are presented as mean ± SEM. ns, not significant; * $P < 0.05$, ** $P < 0.01$, *** $P < 0.001$.
PD-1, programmed cell death protein 1; mAb, monoclonal antibody; SREBP1, sterol regulatory element binding proteins1; KPC, KrasG12D/Trp53R172H/Pdx1-Cre; GZMB, granzyme B; KEGG, Kyoto Encyclopedia of Genes and Genomes; shNC, shRNA negative control; IFN-$\gamma$, interferon-$\gamma$; IHC, immunohistochemistry; OE, overexpression; SEM, standard error of the mean.

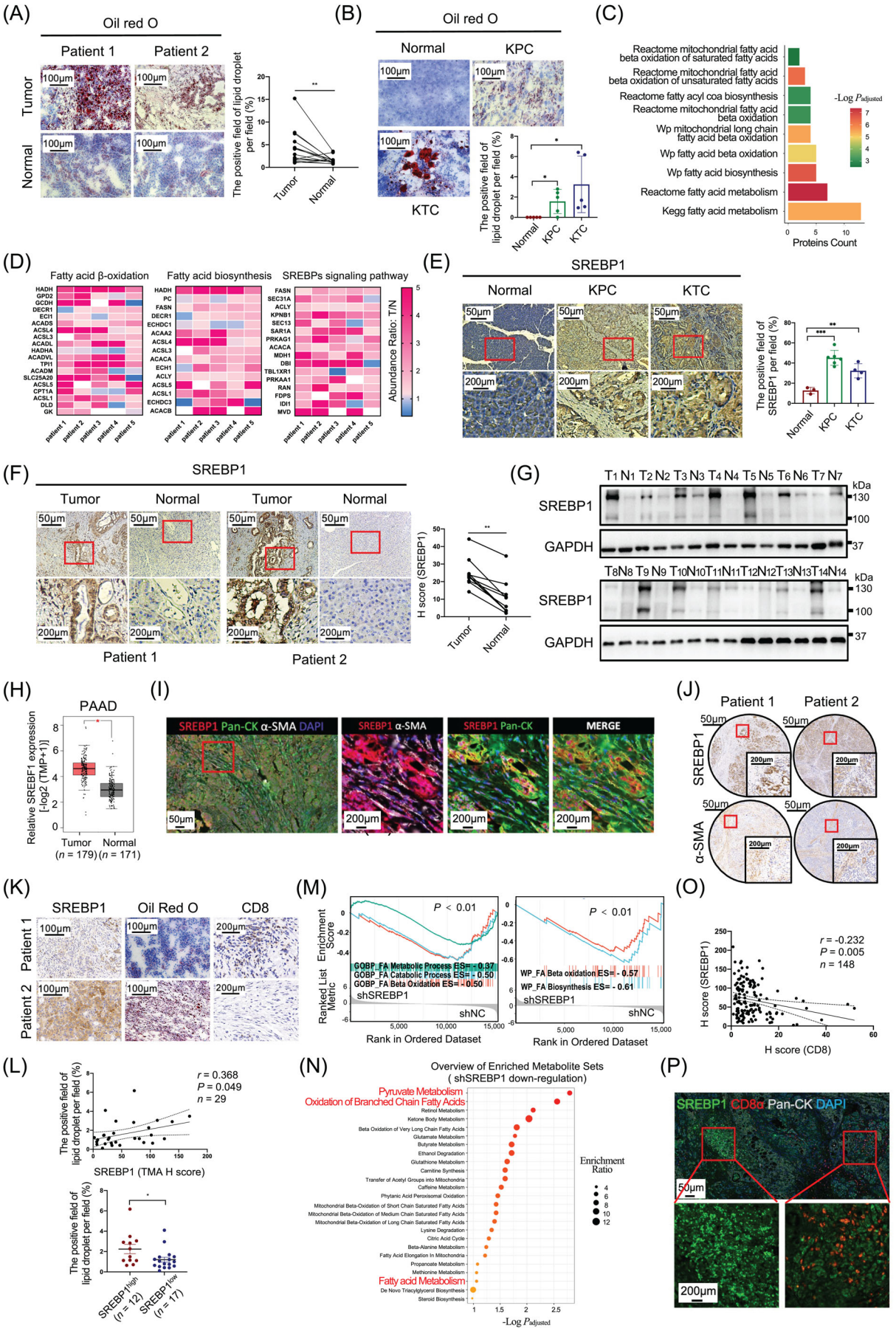

cells exhibited a notable downregulation of genes associated with fatty acid metabolic and catabolic process (Figure 2M).

SREBP1 is capable of encoding the mRNA of key enzymes involved in fatty acid synthesis [26, 27]. Western blotting analysis confirmed that SREBP1 deficiency or Fatostatin treatment decreased the protein levels of enzymes involved in de novo lipogenesis (SCD1, ACACA, FASN) in PDAC cells (Supplementary Figure S3J). GC-MS analysis found that SREBP1 downregulation reduced the cellular abundance of palmitoleic and oleic acids in KPC cells (Supplementary Figure S3K). The metabolomic analysis further confirmed that SREBP1 deficiency inhibited lipid acid metabolism and pyruvate metabolism (Figure 2N and Supplementary Figure S3L), which is attributed to energy metabolism disequilibrium. In addition, SREBP1 levels correlated negatively with the number of $CD8^+$ T cells in pancreatic cancer tissue, as analyzed using a PDAC tissue microarray (Figure 2O-P). These data indicated that SREBP1-dependent fatty acid metabolism was activated in cancer cells, potentially contributing to the formation of an immunologically "cold" TME in PDAC.

### 3.3 | SREBP1 downregulation in PDAC triggered PD-L1 expression and impeded T cell functionality in vivo

Previous studies have demonstrated that the ablation of SREBP1 inhibited the proliferation of human pancreatic cancer cells [28, 29]. We confirmed that SREBP1 deficiency significantly inhibited the proliferation, migration, and invasion of PDAC cells (Supplementary Figure S4A-B). Moreover, we inoculated mouse PDAC cells into immunodeficient BALB/c nude mice. A stable knockdown of SREBP1 led to a significant reduction in the size of orthotopic PDAC tumors and prolonged survival time compared to the control group (Figure 3A-B). Similarly, treatment with Fatostatin resulted in significantly inhibited tumor growth and prolonged survival time compared to the control group (Supplementary Figure S4C-H), with no significant change in body weight observed (Supplementary Figure S4I-J). Thus, targeting SREBP1 suppressed PDAC cell proliferation, invasion, and metastasis in vitro and in vivo.

To assess the role of an intact immune system in the shSREBP1-mediated antitumor effect, we orthotopically inoculated PANC02 mouse PDAC cells into immune-competent C57BL/6 mice. Contrary to the antitumor effects observed in immune-deficient mice with SREBP1 knockdown, there were no significant differences in tumor growth and survival between the shSREBP1 groups and the control group (Figure 3C-D). Using flow cytometry, we found that the activity of infiltrated $CD8^+$ T cells ($Ki67^+$, $GZMB^+$, and IFN-$\gamma^+$) was significantly decreased, while the number of $CD8^+$ T cells, $FoxP3^+$ regulatory T cells, and $CD206^+$ TAMs remained unchanged in the shSREBP1 groups (Figure 3E and Supplementary Figure S5A). IHC also confirmed the flow cytometry results, showing a significant reduction in activated tumor-infiltrated $CD8^+$ T ($GZMB^+$) cells in the shSREBP1 group (Figure 3F). Since tumor PD-L1 engagement with PD-1 on T cells can evade antitumor immunity [30], we hypothesized that the downregulation of SREBP1 might induce immune escape mediated by PD-L1. To test this, we performed flow cytometry, IHC and Western blotting on isolated tumors from

**FIGURE 2** Activation of fatty acid metabolism and its core regulator, SREBP1, in PDAC. (A) Representative images showing the lipid droplet expression profile in paired pancreatic tumor and normal tissues by Oil Red O staining ($n = 15$). (B) Lipid droplet expression profiles in KPC and KTC mouse pancreatic tumors and normal mouse pancreas tissues by Oil Red O staining ($n = 5$). (C) Enrichment analysis of proteomics in 5 pairs of PDAC samples reveals 9 upregulated fatty acid metabolism-related pathways (logFC > 1, $P_{adjusted}$ <0.05). (D) Differential expression of proteins related to fatty acid beta-oxidation (Left), Fatty acid biosynthesis (Middle), and SREBPs signaling pathway (Right) in 5 pairs PDAC samples. (E) SREBP1 expression profiles in KPC ($n = 6$), KTC ($n = 4$) mouse pancreatic tumors, and normal mouse pancreas ($n = 3$) tissues by IHC. (F) SREBP1 expression in paired pancreatic tumor and normal tissues ($n = 10$) by IHC. (G) Western blotting analysis of SREBP1 levels in clinical pancreatic tissue samples from 14 patients. (H)The relative SREBF1 expression in pancreatic cancer and normal pancreatic tissues was analyzed using RNA-seq datasets of PAAD from the TCGA database ($n = 350$). (I) Tissue-based multi-color IHC for SREBP1 (red), Pan-CK (green), α-SMA (white), and DAPI (blue) in human PDAC tissues. (J) Representative images of IHC staining of SREBP1 and α-SMA expression in human PDAC tissues array. (K) The representative images between SREBP1 expression, lipid droplets ($n = 29$), and $CD8^+$ T cell infiltration ($n = 148$), respectively, in human PDAC tissues. (L) The quantifications of SREBP1 expression and lipid droplets in human PDAC tissues. (M) GSEA of Fatty acid metabolism-related signaling pathways in shSREBP1 KPC cells and control. (N) Enrichment analysis of Metabolome in shSREBP1 KPC cells and control. (O) The quantifications of SREBP1 expression and $CD8^+$ T cell infiltration in human PDAC tissues. (P) Tissue-based multi-color IHC for SREBP1 (green), Pan-CK (white), CD8α (red), and DAPI (blue) in human PDAC tissues. Results are presented as mean ± SEM. ns, not significant; $P > 0.05$, $^*P < 0.05$, $^{**}P < 0.01$, $^{***}P < 0.001$.
SREBF1, sterol regulatory element binding transcription factor 1; PDAC, pancreatic ductal adenocarcinoma; IHC, immunohistochemistry; RNA-seq, RNA sequencing; PAAD, pancreatic adenocarcinoma; TCGA, the Cancer Genome Atlas; Pan-CK, pan-cytokeratin; α-SMA, alpha-smooth muscle actin; GSEA, Gene Set Enrichment Analysis; DAPI, 4',6-diamidino-2-phenylindole.

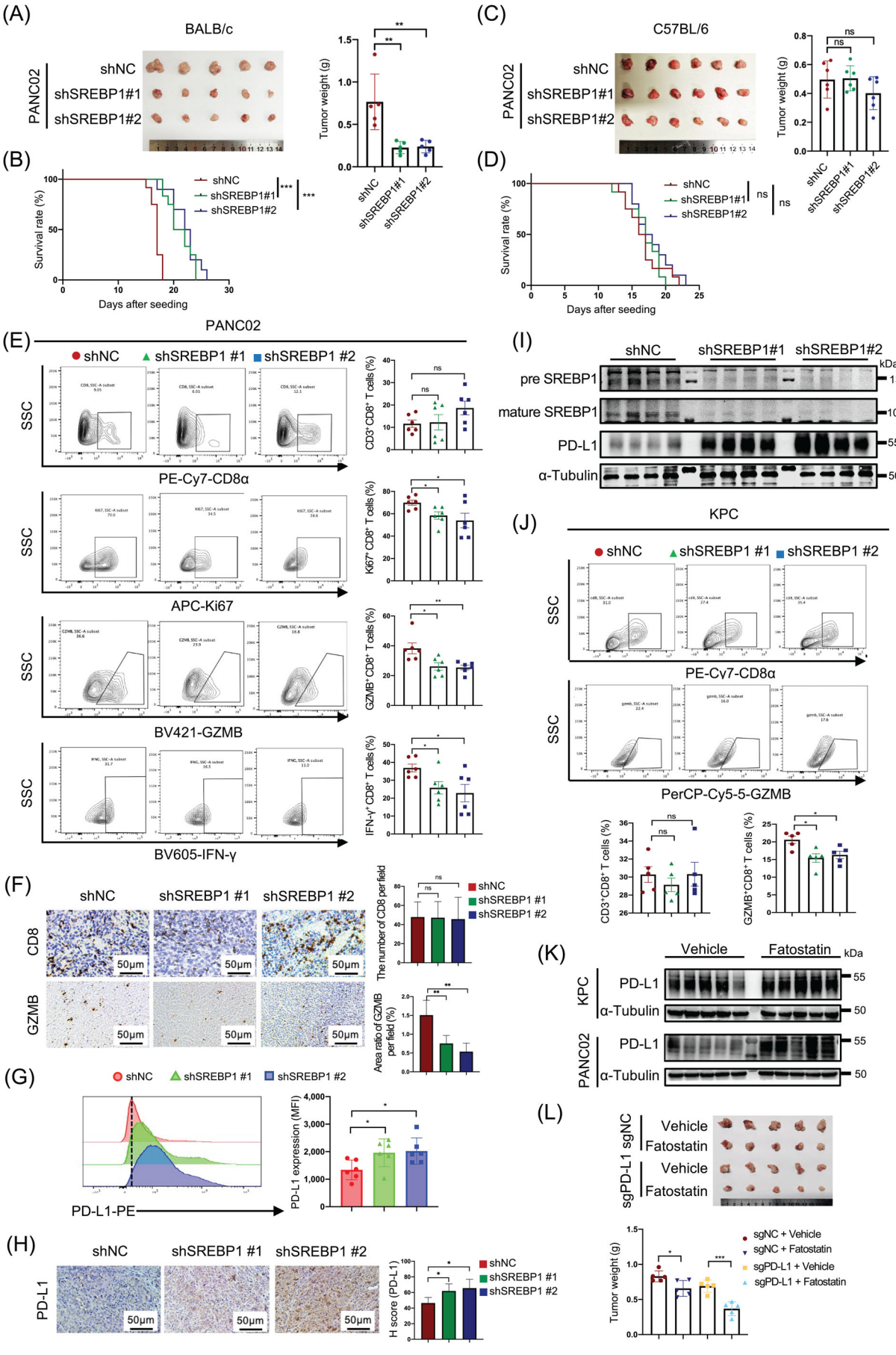

immune-competent C57BL/6 mice, and found a significant upregulation of PD-L1 expression in tumor cells in the shSREBP1 group (Figure 3G-I).

Next, we processed the pancreatic tumor specimens from C57BL/6 mice that had been orthotopically injected with KPC cells (Figure 1M). The activity ($GZMB^+$) and number of infiltrated $CD8^+$ T cells, as well as PD-L1 protein levels in the tumor, were found to be similar to those observed in the PANC02 mouse model (Figure 3J and Supplementary Figure S5B-E). Moreover, in the Fatostatin-treated group, there was an upregulation of PD-L1 protein levels compared to the control group (Figure 3K and Supplementary Figure S5F). Furthermore, Fatostatin was administered to mice bearing sgPD-L1 KPC tumors. Compared to the tumor-inhibiting effect of Fatostatin treatment in sgNC KPC tumors, a more pronounced effect was observed in the sgPD-L1 group (Figure 3L). Together, these findings suggested that downregulation of SREBP1 induced PD-L1 expression, thereby conferring immune evasion capabilities on PDAC cells.

## 3.4 | SREBP1 negated PD-L1 expression in vitro and human PDAC tissues

Targeting SREBP1-mediated upregulation of tumor PD-L1 expression was further validated in PDAC cell lines in vitro. We demonstrated that PD-L1 mRNA and protein levels were significantly higher in the shSREBP1 groups than in the shNC group (Figure 4A-D). Furthermore, using CRISPR/Cas9, we validated that PD-L1 protein levels in the sgSREBP1 groups were significantly higher than in the control group (Figure 4E). Consistently, we showed that Fatostatin enhanced PD-L1 expression in PDAC cell lines, compared to DMSO-treated controls (Figures 4F-H). In contrast, overexpression of SREBP1 significantly reduced PD-L1 levels in mouse and human PDAC cell lines in vitro (Supplementary Figure S6A-B). To further investigate the role of SREBP1 in immune regulation, KPC-OVA and PANC02-OVA cells were co-cultured with T lymphocytes from OT1 mice (OT1-T cells). We demonstrated that the downregulation of SREBP1 in mouse PDAC cells increased their resistance to killing by OT1-T cells in T cell-mediated tumor cell-killing assays (Figure 4I), while overexpression of SREBP1 enhanced the cytotoxicity of OT1-T cells against mouse PDAC cells (Supplementary Figure S6C). In PD-L1-knockout KPC cells, SREBP1 deficiency no longer induced upregulation of PD-L1 expression (Supplementary Figure S6D-E). In addition, cholesterol upregulated the PD-L1 protein level by binding to SREBP cleavage-activating protein (SCAP) (Supplementary Figure S6F), thereby inhibiting the maturation of SREBP1 [31].

We further assessed the protein levels of SREBP1 and PD-L1 in PDAC patient samples to validate our findings in human cancer patient samples. The results showed a negative correlation between SREBP1 and PD-L1 levels (Figure 4J-K). Analysis of the TCGA PDAC database revealed a negative correlation between *SREBF1* and *CD274* at the transcriptional level (Figure 4L). RNA-seq analysis revealed a slight upregulation of *Cd274* following *Srebf1* knockdown in KPC and PANC02 cells (Supplementary Figure S6G). To investigate whether *CD274* is a direct *SREBF1* target gene, we predicted putative *SREBF1*-binding sites within the *CD274* promoter regions with a length of 2,000 bp using JASPAR. ChIP assay identified two and three putative *SREBF1*-binding sites in the *CD274* promoter in mouse and human PDAC cells, respectively (Supplementary Figure S6H). A dual luciferase assay confirmed that one of these binding sites was critical for *SREBF1*-induced *CD274* transactivation in 293T cells (Supplementary Figure S6I-J). We postulated that *SREBF1* inhibited *CD274* transcription by blocking other transcription factors from binding to the *CD274* promoter. A dual luciferase assay confirmed that the *SREBF1*-binding site overlaps with those of *NF-κB* and *STAT3* (Supplementary Figure S6K-L). Our experiments indicated that *SREBF1*

**FIGURE 3** Genetic inhibition of tumor SREBP1 induced tumor PD-L1 expression and was associated with an attenuated suppressive effect on tumor growth. (A-B) The visual maps of tumors and tumor weight (A) of shNC and two shSREBP1 (#1 and #2)-transfected PANC02 xenografts in BALB/c nude mice and Kaplan-Meier survival curves (B) for these mice (5 mice per group). (C-H) The visual maps of tumors and tumor weight (C) of shNC and two shSREBP1 (#1 and #2)-transfected PANC02 xenografts in C57BL/6 mice and Kaplan-Meier survival curves (D) for these mice (6 mice per group). (E) Flow staining and frequency of tumor-infiltrating lymphocytes ($CD8^+$ T cells, $GZMB^+$ $CD8^+$ T cells, $Ki67^+$ $CD8^+$ T cells, and IFN-$\gamma^+$ $CD8^+$ T cells) in indicated PAN02 tumors. (F) IHC staining was performed for CD8 and GZMB in shSREBP1 and shNC PANC02 xenograft tumor samples. (G-I) Representative images and statistical results of tumor PD-L1 expression were shown as indicated by flow cytometry (G), IHC staining (H) and Western blotting (I). (J) Flow staining and frequency of tumor-infiltrating lymphocytes ($CD8^+$ T cells, $GZMB^+$ $CD8^+$ T cells) in indicated KPC tumors. (K) Fatostatin induced the up-regulation of PD-L1 expression in tumor by Western blotting analysis. (L) Tumor image and statistical analysis of C57BL/6 mice implanted with $7\times10^5$ sgNC or sgPD-L1 KPC cells and treated with Fatostatin or vehicle.

Results are presented as mean ± SEM. ns, not significant; $P > 0.05$, $^*P < 0.05$, $^{**}P < 0.01$, $^{***}P < 0.001$.

shNC, shRNA negative control; SREBP1, sterol regulatory element binding protein 1; IHC, immunohistochemistry; GZMB, granzyme B; PD-L1, programmed death-ligand 1; sgNC, single-guide RNA negative control.

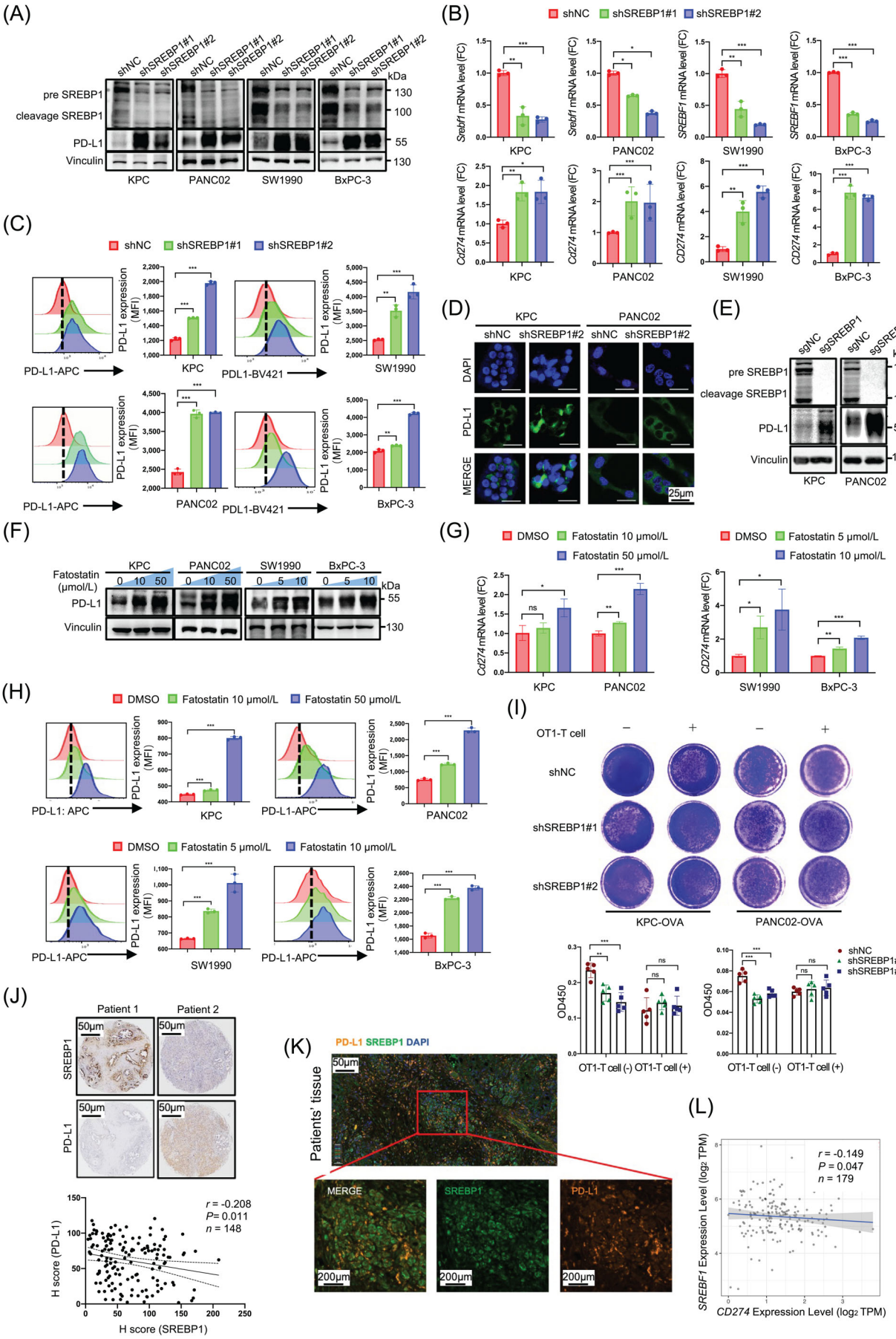

binds directly to the *CD274* promoter to inhibit *CD274* transcription.

## 3.5 | *PCSK9* was a direct transcriptional target of *SREBF1* to induce immunosuppression and neoplasia in PDAC

Given that the direct transcriptional regulation of PD-L1 by SREBP1 is weak, as evidenced by RNA-seq analysis of KPC and PANC02 cells (log2FC < 1.0), we hypothesized the existence of additional mechanisms for the regulation of PD-L1 by SREBP1. SREBP1-OE and control SW1990 cells underwent CUT & Tag sequencing. PCSK9 was identified as the top candidate based on expression fold change among all the candidate proteins interacting with PD-L1 (Figure 5A and Supplementary Figure S7A-B). RNA-seq analysis revealed significant downregulation of *Pcsk9* following *SREBF1* knockdown in KPC and PANC02 cells (Figure 5B). We validated that shSREBP1 significantly reduced tumor PCSK9 levels in mouse and human PDAC cell lines using Western blotting and qRT-PCR (Figure 5C-D). ELISA confirmed that knockdown of SREBP1 decreased PCSK9 levels in the culture supernatant of mouse PDAC cells (Figure 5E). In contrast, overexpression of SREBP1 increased PCSK9 protein levels in PDAC cells (Supplementary Figure S7C). Fatostatin decreased the levels of PCSK9 mRNA and protein in PDAC cells, as well as the amount of PCSK9 protein secreted from PDAC cells (Figure 5F-G and Supplementary Figure S7D). To investigate whether *PCSK9* is a direct SREBF1 target gene, we searched for potential *SREBF1*-binding sites in the human *PCSK9* gene promoter region (Supplementary Table S5). A ChIP-qPCR assay confirmed that SREBP1 was directly bound to three potential binding sites in the *PCSK9* promoter in human PDAC cells (Figure 5H and Supplementary Figure S7E). The dual luciferase assay confirmed that the three SREBF1-binding sites were critical for SREBF1-induced *PCSK9* transactivation (Figures 5I-J).

PCSK9 expression showed a positive correlation with SREBP1 levels, as determined by IHC and mIHC analysis of PDAC tissues, corroborated by data from the TIMER database (Figures 5K-M). In agreement with the SREBP1-mediated immunosuppressive TIME in PDAC, PCSK9 expression inversely correlated with $CD8^+$ T cell infiltration in human PDAC tissues from the TIMER database (Figure 5N). Low tumor PCSK9 expression predicted better OS in cancer patients with enriched $CD8^+$ T cell infiltration, while in tumors with $CD8^+$ T cell-deficient tumors, tumor PCSK9 expression was not associated with patients' survival (Figure 5O). Patients exhibiting an objective response to anti-PD-1 therapy had lower serum PCSK9 levels compared to those with a non-objective response (Figure 5P). In addition, the expression of PCSK9 was significantly lower in the matched adjacent normal tissues compared with that in cancer tissues according to the Western blotting and IHC results (Supplementary Figure S7F-G). Thus, we present evidence that *SREBF1*-mediated transcription of *PCSK9* contributes to neoplasia and immunological TIME in PDAC.

## 3.6 | PCSK9 functions downstream SREBP1 to drive PD-L1 degradation through the lysosomal pathway

To further confirm that PCSK9 is a regulator of PD-L1 expression, we generated stable models of PCSK9 knockdown in KPC, PANC02 and SW1990 cell lines. Western blotting, flow cytometry, and IF analyses revealed that PCSK9 knockdown significantly increased PD-L1 protein levels in PDAC cells (Figure 6A-C). Consistently, transient knockdown of PCSK9 using siRNAs also elevated PD-L1 levels (Supplementary Figure S7H-I). PF-06446846, a chemical inhibitor, has been previously demonstrated

**FIGURE 4** SREBP1 plays an important role in the negative regulation of PD-L1 expression in PDAC. (A–D) Analysis of PD-L1 expression in PDAC cell lines transfected with shSREBP1 or shNC. (A) Western blotting analysis of SREBP1 and PD-L1 expression; (B) RT-PCR analysis of *SREBF1* and *CD274* expression; (C) FACS of $PD\text{-}L1^+$ membrane expression; and (D) IF staining of PD-L1. (E) Western blotting analysis of PD-L1 expression of KPC and PANC02 transfected with sgSREBP1 or sgRNA. (F–H) Analysis of PD-L1 expression of PDAC cell lines treated with or without Fatostatin at the indicated doses for 48 h. (F) Western blotting analysis of PD-L1 expression; (G) RT-PCR analysis of *CD274* expression, and (H) FACS of $PD\text{-}L1^+$ membrane expression. (I) Representative images (Top) and statistical results (Bottom) of OT1-T cell-mediated cancer cell-killing assay results ($n = 5$). (J) Representative images (Top) and statistical result (Bottom) of IHC staining of SREBP1 and PD-L1 expression in a PDAC tissue array. (K) Tissue-based multi-color IHC for SREBP1 (green), PD-L1 (orange), and DAPI (blue) in human PDAC tissues. (L) *SREBF1* is negatively correlated with *CD274* in pancreatic cancer from the TCGA-PAAD database. Results are presented as mean ± SEM, $n = 3$. And all results were repeated for three times. ns, not significant; $P > 0.05$, $^*P < 0.05$, $^{**}P < 0.01$, $^{***}P < 0.001$. PDAC, pancreatic ductal adenocarcinoma; SREBP1, sterol regulatory element binding protein 1; shNC, shRNA negative control; PD-L1, programmed death-ligand 1; RT-PCR, reverse transcription polymerase chain reaction; CD274, cluster of differentiation 274; FACS, fluorescence-activated cell sorting; IF, immunofluorescence; sgRNA, single-guide RNA; IHC, immunohistochemistry; DAPI, 4',6-diamidino-2-phenylindole; TCGA-PAAD, the Cancer Genome Atlas - Pancreatic Adenocarcinoma.

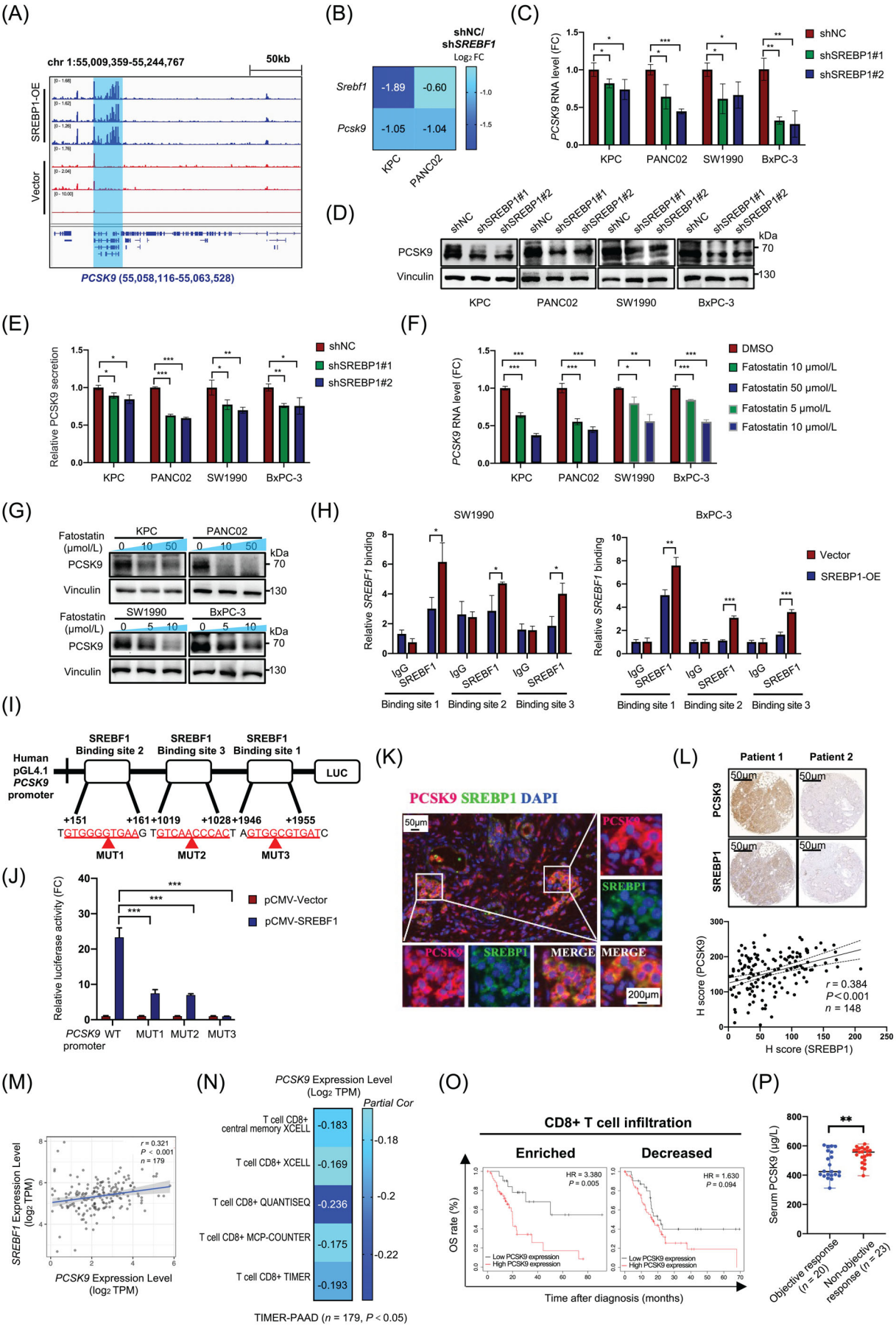

to effectively inhibit mouse PCSK9 expression by reducing PCSK9 translation [32]. Furthermore, treating PDAC cell lines with PF-06446846 resulted in outcomes similar to those observed with shPCSK9 (Figure 6D-E).

How does PCSK9 regulate cell surface PD-L1 expression? Liu X et al. demonstrated that PCSK9 promoted lysosome-mediated degradation of MHC-I in tumor cells [33]. Our analysis indicated that PCSK9 deficiency increased MHC-I alloantigen levels in PDAC cell lines, but the increase was less significant than that observed for PD-L1 (Supplementary Figure S7J-K). Thus, it is crucial to explore the relationship between PCSK9 and PD-L1. We postulated that PCSK9 promoted PD-L1 degradation by importing PD-L1 into lysosomes. Firstly, a protein mass spectrometry analysis of SW1990 cells after Co-IP with an anti-PD-L1 antibody identified a PCSK9 peptide, suggesting a possible interaction between PCSK9 and PD-L1 (Figure 6F). Co-IP revealed that endogenous PCSK9 and PD-L1 proteins interacted with each other in KPC and SW1990 cell lines (Figure 6G and Supplementary Figure S7L). In addition, exogenous Flag-PD-L1 and HA-PCSK9 were introduced into 293T, KPC, PANC02, and SW1990 for CoIP, which showed that PD-L1 and PCSK9 formed a complex with either exogenous or endogenous proteins (Figure 6H and Supplementary Figure S7M). Moreover, GST pull-down assay showed that PCSK9 bound to PD-L1 directly (Figure 6I).

To understand how PCSK9 regulates the cell surface expression of PD-L1, we carried out IF co-staining of exogenously expressed PD-L1 and/or PCSK9 in SW1990 cells with PCSK9 knockdown or PCSK9 overexpression. In PCSK9-OE cells, more PD-L1 was localized in the lysosome and less in the plasma membrane, whereas in PCSK9-knockdown cells, PD-L1 staining indicated more significant localization to the plasma membrane (Figure 6J). CHX and Baf-A1 were used to analyze the functional significance of the physical association of PCSK9 and PD-L1 in lysosomes. Without *de novo* protein synthesis (because of CHX treatment), the PD-L1 levels in PCSK9-knockout cells declined more slowly than those in control cells (Figure 6K and Supplementary Figure S7N). When the cells were exposed to Baf-A1 to inhibit lysosome function, PD-L1 levels significantly accumulated in both control cells and PCSK9-knockout cells (Figure 6L). Western blotting analysis of fractionated cellular lysates confirmed that PCSK9-OE caused an increase in PD-L1 protein levels in lysosomes, while PCSK9-knockout decreased the lysosome fraction. By contrast, in the membrane fraction, PCSK9-OE reduced the relative abundance of the PD-L1 protein, while PCSK9-knockout increased it (Figure 6M). To confirm the interaction between PCSK9 and PD-L1, we conducted rigid protein-protein docking of PCSK9 and PD-L1 utilizing the GRAMM-X software, generating 10 distinct sets of docking outcomes. Among these, the initial set represented the optimal docking conformation. This conformation was subsequently visualized and scrutinized using Pymol and LigPlus software. Within the docked region of the two proteins, multiple amino acid residues were interconnected via hydrogen bonding forces, which served to maintain the stable association between PCSK9 and PD-L1 (Figure 6N). These results suggested that PCSK9 is critical in regulating PD-L1 levels via lysosome-mediated degradation.

PDAC cells with PCSK9 knockout were transfected with shSREBP1 to verify the role of PCSK9 in SREBP1-mediated PD-L1 regulation in PDAC cells. Flow cytometry and Western blotting showed that PCSK9 knockout significantly attenuated SREBP1 deficiency-induced upregulation of PD-L1 protein levels (Figure 6O-P). PDAC cells with

**FIGURE 5** SREBP1 binds directly to the PCSK9 promoter in PDAC. (A) Signal densities of CUT & Tag-seq at *PCSK9* gene loci in SW1990 cells, showing *SREBF1* binding. (B) *PCSK9* expression of KPC and PANC02 cells transfected with shSREBP1 or shNC, as determined by RNA-seq analysis. (C-D) RT-PCR (C) and Western blotting (D) analysis of PCSK9 expression of KPC and PANC02 cell transfected with shSREBP1 or shNC. (E) ELISA assay analyzed the Secreted PCSK9 of PDAC cell lines transfected with shSREBP1 or shNC in the culture supernatant. (F-G) qRT-PCR (F) and Western blotting (G) analysis of PCSK9 expression of PDAC cell lines treated with or without Fatostatin at the indicated doses for 48 h. (H) *SREBF1* binding to the *PCSK9* promoter was determined by chromatin immunoprecipitation-RT-PCR in human PDAC cell lines (BxPC3 and SW1990). (I) Schematic representation of the *PCSK9* promoter cloned into the pGL4.1 vector. Three predicted *SREBF1* binding motifs are shown, and promoter constructs containing mutations in these 3 regions to cause SREBF1-binding deficiency are generated. (J) Analysis of *PCSK9* WT or mutant promoter activity in 293T cell lines transfected with SREBF1-Flag. (K-M) SREBP1 is positively correlated with PCSK9 in PDAC by multi-color IHC (K), ordinary IHC (L) and TIMER database (M). (N) The correlation of SREBF1 and $CD8^+$ T cell in PAAD from the TIMER database. (O) Kaplan-Meier analysis of survival in PDAC according to the expression of PCSK9 in the group with decreased or enriched intratumoral $CD8^+$ T cell infiltration. (P) Comparison of serum PCSK9 levels in patients with objective response versus non-objective response to anti-PD-1 therapy ($n = 43$). Results are presented as mean ± SEM, $n = 3$. And all results were repeated for three times. ns, not significant; $P > 0.05$, *$P < 0.05$, **$P < 0.01$, *** $P < 0.001$.

CUT & Tag-seq, cleavage under targets and tagmentation sequencing; SREBF1, sterol regulatory element binding factor 1; shNC, shRNA negative control; RNA-seq, RNA sequencing; ELISA, enzyme-linked immunosorbent assay; qRT-PCR:quantitative reverse transcription polymerase chain reaction; PAAD, pancreatic adenocarcinoma; TIMER, tumor immune estimation resource; IHC, immunohistochemistry; PDAC, pancreatic ductal adenocarcinoma.

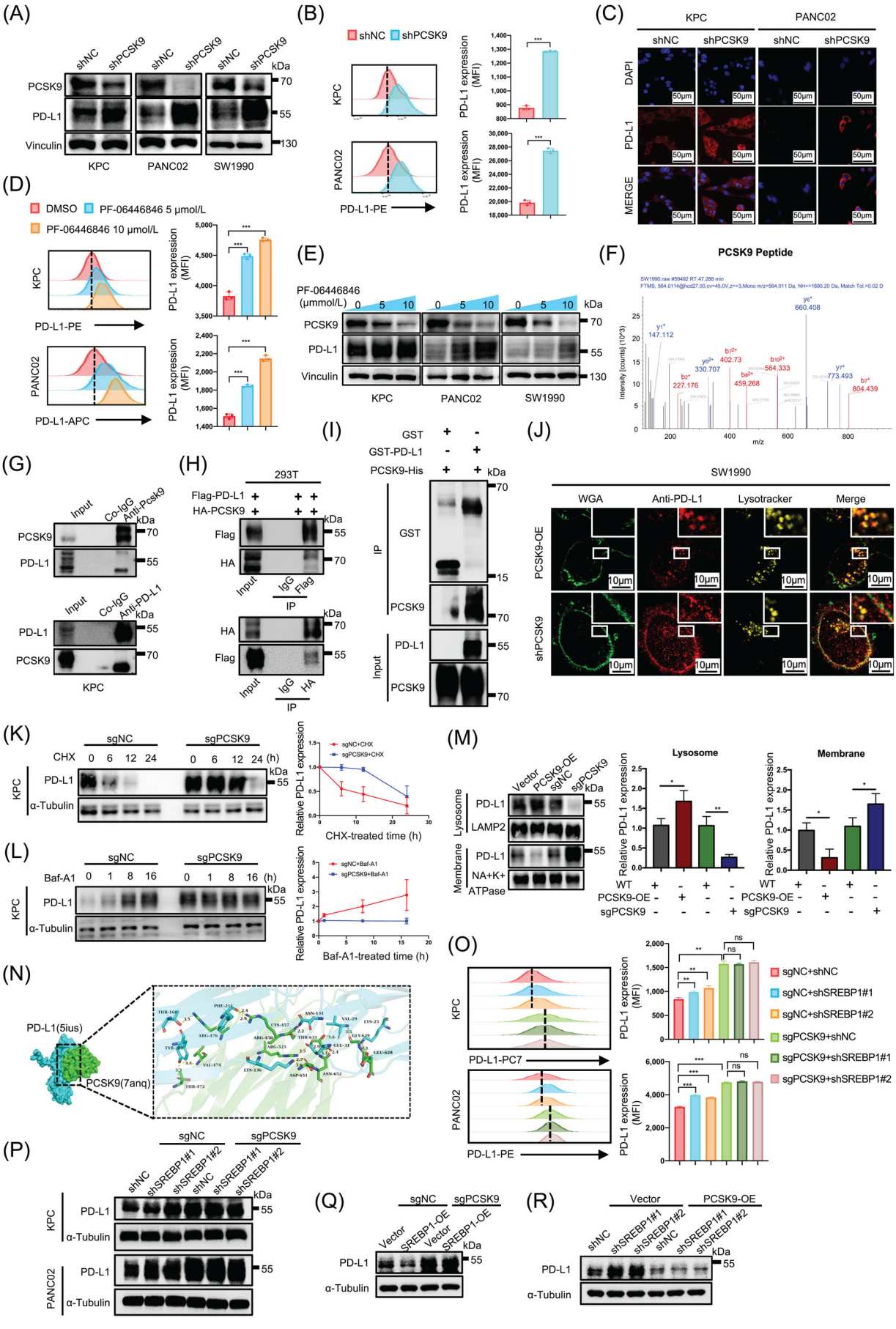

PCSK9 knockout were transfected with a plasmid that carries the *SREBF1* gene, and PD-L1 protein expression did not change (Figure 6Q). Also, PCSK9-OE significantly reduced the PD-L1 protein expression, antagonizing the effects of SREBP1 knockdown (Figure 6R). Given the broad downstream effects of knocking down the master transcriptional regulator of lipogenesis, *SREBF1*, we verified the regulation of PD-L1 by other downstream genes directly transcribed by *SREBF1*. Western blotting analysis showed that the protein level of PD-L1 was unaffected when we knocked out FASN, ACACA and SCD1 in KPC cells, respectively (Supplementary Figure S7O). PD-L1 expression was still upregulated by shSREBP1 in KPC cells with FASN, ACACA, and SCD1 knockout, except for KPC cells with PCSK9 knockout (Supplementary Figure S7P). These data supported the hypothesis that SREBP1 deficiency induced PD-L1 expression by direct transcriptional regulation of PCSK9 expression.

### 3.7 | Preclinical evaluation revealed the augmented antitumor effect of PCSK9 targeting in PDAC immunotherapy

Recent studies have reported that targeting PCSK9 to treat cancer is an attractive immunotherapy on other tumors, increasing MHC-I expression in immune-competent mice models [33, 34]. We found that PCSK9 deficiency mainly induced the cell surface expression of PD-L1 in PDAC cell lines. It is widely conceded that high PD-L1 expression results in a better therapeutic outcome in response to PD-1 mAb treatment [35]. Thus, targeting PCSK9 to upregulate PD-L1 expression offers promising opportunities for enhancing the therapeutic efficacy of PD-L1-targeted drugs in PDAC. Indeed, shPCSK9 plus PD-1 mAb significantly improved the antitumor effect in vivo compared with PD-1 mAb only (Figure 7A-B and Supplementary Figure S8A-C). Flow cytometry and IHC staining analysis showed that shPCSK9 plus PD-1 mAb therapy significantly increased the tumor-infiltrating cytotoxic $CD8^+$ T cell population (Figure 7C and Supplementary Figure S8D). Compared with shNC group, shPCSK9 significantly increased tumor PD-L1 expression (Figure 7D and Supplementary Figure S8D). Notably, the significant suppression of tumor weight induced by PCSK9 knockdown was reversed following CD8$\alpha$ monoclonal antibody treatment (Figure 7E-F and Supplementary Figure S8E). Besides, cotreatment of PD-1 mAb with Evolocumab or Alirocumab, the China Food and Drug Administration (CFDA)-approved PCSK9 neutralizing antibodies for the treatment of adult patients with primary hypercholesterolemia and mixed dyslipidemia, decreased the PDAC tumor volume and prolonged the survival compared with PD-1 mAb treatment, with no significant differences in body weight and biochemical indexes of liver and kidney functions (Figure 7G-H and Supplementary Figure S8F-H).

To explore the preclinical value of PCSK9 inhibition in combination with PD-1 mAb, we established the PDAC PDX-huPBMC mouse model, and Evolocumab and Pembrolizumab (PD-1 neutralizing antibody) were used to treat PDAC (Figure 7I). The combination therapy significantly accelerated antitumor efficacy compared with monotherapy with Evolocumab or Pembrolizumab (Figure 7J-K). In the combination therapy group, we also observed increased intratumoral $CD8^+$ T cell infiltration and a reversal of $CD8^+$ T cell exhaustion (Figure 7L). There was no significant difference in spleen and body weight between vehicle, Evolocumab, Pembrolizumab and Evolocumab + Pembrolizumab groups at the end of treatment (Supplementary Figure S8I-J). In addition, to confirm this conclu-

**FIGURE 6** The SREBP1-PCSK9 axis promotes the lysosomal degradation of PD-L1 in PDAC cells. (A–C) Analysis of PD-L1 expression of PDAC cell lines transfected with shPCSK9 or shNC by western blotting (A), flow cytometry (B), and IF (C). (D-E) Flow cytometry (D) and western blotting (E) analysis of PD-L1 expression of PDAC cell lines treated with or without PF-06446846 (PCSK9 inhibition) at the indicated doses for 48 h. (F) PCSK9 peptide fragment was precipitated with PD-L1 Ab by mass spectrometry. (G) Western blotting of coIP of endogenous PCSK9 and PD-L1 in KPC cells. (H) 293T cells were transfected with the indicated plasmids, followed by coIP using FLAG or HA antibodies. (I) GST-pull down assay of PCAK9-His and GST-PD-L1 protein. (J) Representative fluorescence confocal images of PD-L1 distribution were shown in PCSK9-overexpressing or PCSK9-knockdown SW1990 cells. (K-L) Western blotting analysis of PD-L1 expression of PCSK9 knockout KPC cells treated with 20 μmol/L CHX (K) or 50 nmol/L Baf-A1 (L). (M) Western blotting analysis of PD-L1 levels of KPC cell transfected with sgPCSK9, PCSK9-OE, or WT on the cell membrane and lysosome. (N) 3D plot of PCSK9-PDL1 complex interaction by PCSK9 and PD-L1 protein docking analysis. (O-P) Flow cytometry (O) and western blotting (P) analysis of PD-L1 expression of sgPCSK9 KPC and PANC02 transfected with shSREBP1 or shNC. (Q-R) Rescue experiments prove the role of PCSK9 in SREBP1-mediated PD-L1 regulation by western blotting. Results are presented as mean ± SEM, $n = 3$. And all results were repeated for three times. ns, not significant; $P > 0.05$, $^*P < 0.05$, $^{**}P < 0.01$, $^{***}P < 0.001$.

SREBP1, sterol regulatory element binding protein 1; PCSK9, proprotein convertase subtilisin/kexin type 9; PD-L1, programmed death-ligand 1; PDAC, pancreatic ductal adenocarcinoma; shNC, shRNA negative control; IF, immunofluorescence; Ab, Antibody; coIP, co-immunoprecipitation; HA, hemagglutinin; GST, glutathione S-transferase; CHX, cycloheximide; Baf-A1, bafilomycin A1; OE, overexpression; WT, wild type.

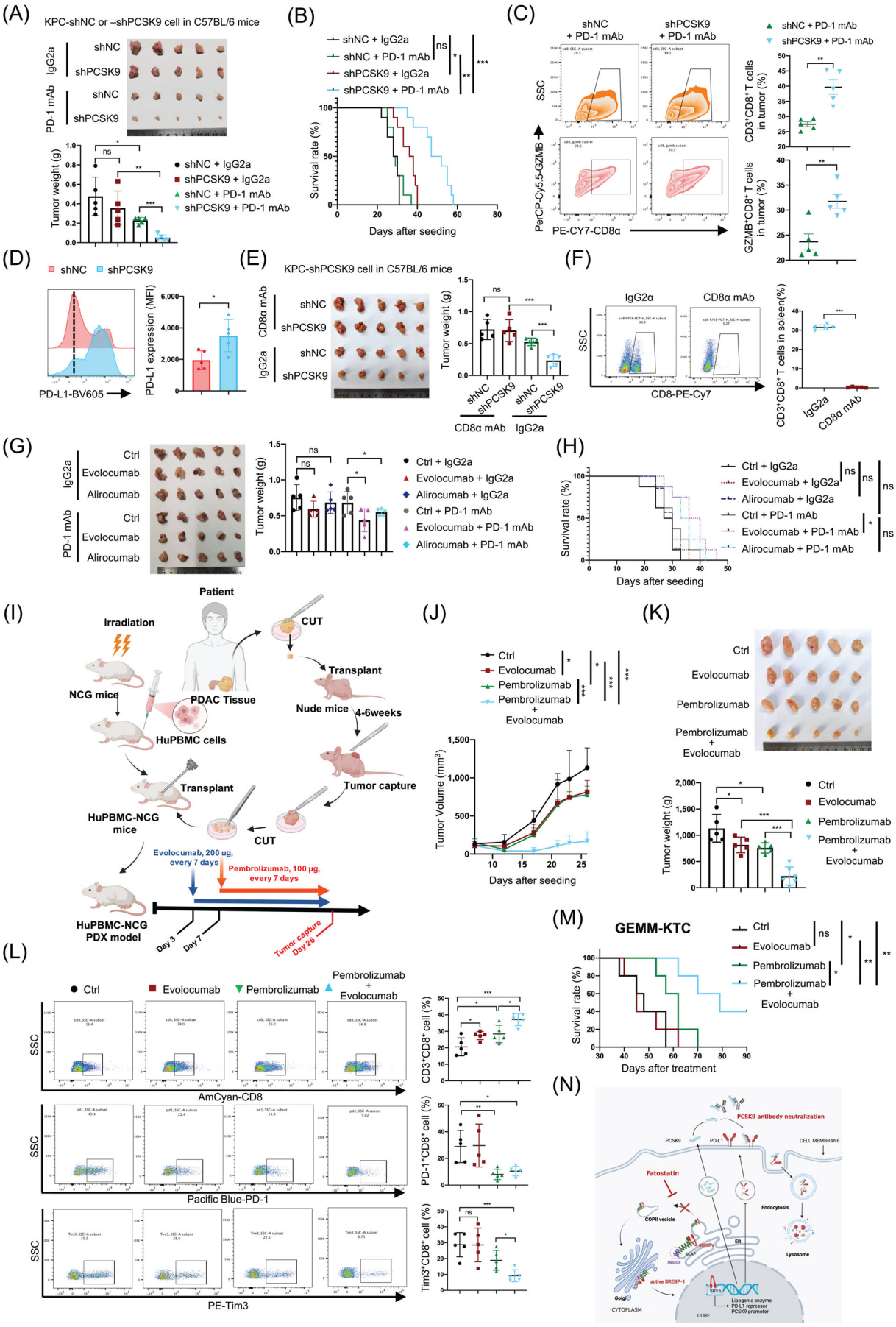

sion in a genetic model, we used an autochthonous model of mutation (GEMM-KTC model). The survival of the mice treated with the antibody combination was prolonged significantly compared with the isotype control-treated mice (Figure 7M). These preclinical results suggest that combining anti-PCSK9 and anti-PD-1 provides a rational and effective strategy for comprehensive PDAC therapy.

## 4 | DISCUSSION

Advanced PDAC appears to derive limited benefits from anti-PD-1 therapies. Our study revealed a robust association between the activation of lipid metabolism and resistance to anti-PD-1 therapy, which was associated with an unfavorable prognosis in PDAC patients. We found that SREBP1 exacerbated the reprogramming of lipid metabolism, enhanced the immunosuppressive TME, and induced resistance to anti-PD-1 therapy in PDAC. Specifically, SREBP1 directly transcribed PCSK9, which can disrupt the recycling of PD-L1 to the cell surface by physically engaging with it and promoting its translocation and degradation in lysosomes. Consequently, targeting the SREBP1-PCSK9 axis to modulate lipid metabolism may suppress tumor growth and alleviate tumor immunosuppression in PDAC.

Evidence suggests that aberrant lipid metabolism is associated with tumor cell adaptation to the TME. Recent studies have primarily focused on the impact of lipid metabolism in tumor cells on the non-immune progression, the effects of lipid metabolism in tumor-infiltration immune cells on TIME and the therapeutic effects of cancer immunotherapies [12, 14, 36-40]. However, few studies have investigated the effect of abnormal lipid metabolism of tumor cells on the remodeling of the TIME and immunotherapy [41]. In pancreatic cancer, we reported inhibition of lipid metabolism remodeling of the tumor immunosuppressive environment by stimulating PD-L1 expression, thereby improving tumor immunotherapy. Based on the above analysis, abnormal lipid metabolism might be closely related to the low expression of PD-L1 and the number of tumor-infiltrating $CD8^+$ T cells in pancreatic cancer. In other words, aberrant lipid metabolism is the main cause of PD-L1 deficiency, which further leads to the "immune desert" of pancreatic cancer. Therefore, remodeling lipid metabolism might represent a new direction to solve the immune tolerance of pancreatic cancer and increase the efficacy of immunotherapy.

In addition, obese patients with tumors often have abnormal lipid metabolism. As expected, recent research demonstrated that obesity impairs $CD8^+$ T cell function in the TME and suppresses antitumor immunity [36, 42, 43]. These findings highlighted that obesity is a biomarker for some cancer immunotherapies, and blocking lipid metabolic reprogramming in tumor cells in obese patients improves antitumor immunity. However, another study revealed that obesity is positively associated with the efficacy of PD-1/PD-L1 blockade in both tumor-bearing mice and clinical cancer patients [44].

**FIGURE 7** The combined effect of targeting PCSK9 and PD-1 mAb combination treatment is dependent on $CD8^+$ T cells. (A-D) C57BL/6 mice were implanted with $7\times10^5$ shPCSK9 or shNC KPC cells received PD-1 mAb or IgG2a control. (A) Tumor image and statistical analysis of orthotopic PDAC model (5 mice/group). (B) Kaplan-Meier survival curves for each group (10 mice/group). (C-D) Flow cytometry showing tumor-infiltrating lymphocytes ($CD8^+$ T cells, $GZMB^+CD8^+$ T cells) and tumor cell PD-L1 expression. (E-F) C57BL/6 mice were implanted with $7\times10^5$ shPCSK9 KPC or shNC cells received PD-1 mAb or CD8α mAb treatment. (E) Tumor image and statistical analysis of orthotopic PDAC model (5 mice/group). (F) Flow cytometry and quantification of $CD8^+$ splenocytes confirming immune cell depletion. (G-H) C57BL/6 mice were implanted with $7\times10^5$ KPC cells and co-treated with PCSK9 neutralizing antibodies (Evolocumab or Alirocumab) and PD-1 mAb. (G) Tumor image and statistical analysis of orthotopic PDAC model (5 mice/group). (H) Kaplan-Meier survival curves for each group (10 mice/group). (I-L) The HuPBMC-NCG PDX model was co-treated with PCSK9 neutralizing antibodies and PD-1 mAb. The schematic diagram shows the process of constructing the patient-derived PDAC-huPBMC mice model (Top) and treatment schedule (Bottom). (J-K) Plots of tumor growth (J) and tumor weight (K) for each group (5 mice/group). (L) Representative images and statistical results of tumor-infiltrating lymphocytes ($CD8^+$ T cells, $PD1^+CD8^+$ T cells, and $Tim3^+CD8^+$ T cells) are shown as indicated by flow cytometry. (M) Kaplan-Meier survival curves for tumor-bearing GEMM mice co-treated with PCSK9 neutralizing antibodies and PD-1 mAb. Treatments began when the solid tumor was palpable. (N) Diagram illustrating SREBP1-mediated PD-L1 regulation. SREBP1 binds to the PD-L1 promoter to suppress its transcription. Meanwhile, SREBP1 binds to the PCSK9 promoter to promote its transcription, then PCSK9-mediated degradation of PD-L1 in the lysosome. Fatostatin (red arrows) impairs the activation of SREBP-1 by inhibiting the ER-Golgi translocation of SREBPs, which increases the PD-L1 expression.

Results are presented as mean ± SEM. ns, not significant; $P > 0.05$, $^*P < 0.05$, $^{**}P < 0.01$, $^{***}P < 0.001$.

PD-1, programmed death-1 monoclonal antibody; mAb, monoclonal antibody; IgG2a, immunoglobulin G2a; PDAC, pancreatic ductal adenocarcinoma; shNC, shRNA negative control; PD-L1, programmed death-ligand 1; GZMB, granzyme B; HuPBMC, human peripheral blood mononuclear cells; PDX, patient-derived xenograft; GEMM, genetically engineered mouse model; ER-Golgi:Endoplasmic Reticulum – Golgi; SREBP1, sterol regulatory element binding protein 1; Tim3, T-cell immunoglobulin and mucin-domain containing-3.

These data indicate a complex and paradoxical impact of obesity on cancer. However, more clinical data is required to confirm the contradictory results in pancreatic cancer. To gain a deeper understanding of obesity or lipid metabolism in cancer, we need to analyze patients with different stages of cancer separately. Cancer cachexia is often associated with advanced pancreatic cancer [45]. While muscle loss has long dominated cachexia research, recent research has begun to recognize the development and progression of cancer cachexia related to lipid metabolism alterations [46]. Thus, the effects of lipid metabolism on the tumor immune response and the efficacy of immunotherapy are complex in patients with different stages of cancer. These results suggest that lipid metabolism in patients with early-stage tumors might be a biomarker of immunotherapy response; however, with the appearance of cachexia in tumor progression, lipid metabolism loses its relevance to antitumor immunity and immunotherapy.

A large number of preclinical studies have demonstrated that neutralizing PCSK9 might promote intratumoral infiltration by T cells and thus render tumors more responsive to immune checkpoint therapy [33, 47-49]. Interestingly, herein, we reported that *PCSK9* might be a key factor that regulates PD-L1 by serving as a direct transcriptional target of SREBF-1 in pancreatic cancer. Furthermore, clinical studies have evaluated the safety of evolocumab or alirocumab (PCSK9 blockade therapy), and evolocumab or alirocumab are ideal as clinically combined immunotherapy agents [50–52]. Our study confirmed the clinical value of anti-PCSK9 in treating pancreatic cancer. It also makes targeted SREBP1-sensitized pancreatic cancer immunotherapy have the value of clinical transformation.

However, the present study had some limitations. The abnormal lipid metabolism exists not only on tumor cells but also on immune cells. However, the function of lipid metabolism on immune cells was not investigated. The clinical value of anti-PCSK9 and Fatostatin in treating pancreatic cancer needs to be confirmed by further clinical studies.

## 5 | CONCLUSIONS

The study indicated that SREBP1 played an important role in regulating PD-L1 expression levels via PCSK9-mediated lysosome degradation and transcription in PDAC. We also discovered that targeting the SREBP1-PCSK9 axis reshaped the TME and enhanced the efficacy of anti-PD-1 therapy. Moreover, a combination of PCSK9 neutralizing antibodies and anti-PD-1 monotherapy showed a favorable antitumor effect in humanized PDX model. Thus, our research proposed a promising combination treatment strategy of anti-PD-1 and lipid metabolism targeting.

## AUTHOR CONTRIBUTIONS

X.B., and T.L. supervised the study; X.Z. and M.L. conceptualized the research and experimental design; M.L., X.Z., Z.L., K.S., H.Y., S.W., L.H., Y.C., H.Z. and J.S. conducted the experiments; M.L. and X.Z. conducted data analyses and interpretation; M.L. and X.Z. wrote the draft; D.X. contributed to technical assistance; X.Z. and X.B. revised the manuscript. All authors read and approved the final version of the manuscript.

## ACKNOWLEDGMENTS

This work was supported by grants from the National Natural Science Foundation of China (U20A20378, 82188102, 81830089 to TBL, 82071867, U23A20462 to XLB); the Key Research and Development Program of Zhejiang Province (2019C03019 to TBL, 2020C03117 to XLB); and "Ling Yan" Research and Development Program of Department of Zhejiang Province Science and Technology (2024C03167 to XLB).

## CONFLICT OF INTEREST STATEMENT

The authors have no conflicts of interest to declare.

## ETHICS APPROVAL AND CONSENT TO PARTICIPATE

This study was approved by the Institutional Review Board at First Affiliated Hospital, School of Medicine, Zhejiang University (Approval No. 2024-726). All participants provided informed written consent.

## DATA AVAILABILITY STATEMENT

The RNA-seq data from shNC and shSrebf1 KPC/PANC02 cells (GSE290259), as well as the CUT&Tag data from Vector and SREBP1 overexpressing SW1990 cells (GSE292417), have been deposited in the GEO database. Other data supporting the findings of this study are available from the corresponding author upon request.

## ORCID

*Mengyi Lao* https://orcid.org/0000-0003-3650-5345
*Tingbo Liang* https://orcid.org/0000-0003-0143-3353
*Xueli Bai* https://orcid.org/0000-0002-2934-0880

## REFERENCES

1. Ho WJ, Jaffee EM, Zheng L. The tumour microenvironment in pancreatic cancer — clinical challenges and opportunities. Nat Rev Clin Oncol. 2020;17(9):527-40.
2. Sharma P, Hu-Lieskovan S, Wargo JA, Ribas A. Primary, Adaptive, and Acquired Resistance to Cancer Immunotherapy. Cell. 2017;168(4):707-23.

3. Zhang Y, Chen L. Classification of Advanced Human Cancers Based on Tumor Immunity in the MicroEnvironment (TIME) for Cancer Immunotherapy. JAMA Oncol. 2016;2(11):1403-4.
4. O'Reilly EM, Oh DY, Dhani N, Renouf DJ, Lee MA, Sun W, et al. Durvalumab With or Without Tremelimumab for Patients With Metastatic Pancreatic Ductal Adenocarcinoma: A Phase 2 Randomized Clinical Trial. JAMA Oncol. 2019;5(10):1431-8.
5. Li H, van der Merwe PA, Sivakumar S. Biomarkers of response to PD-1 pathway blockade. Br J Cancer. 2022;126(12):1663-75.
6. Herbst RS, Soria JC, Kowanetz M, Fine GD, Hamid O, Gordon MS, et al. Predictive correlates of response to the anti-PD-L1 antibody MPDL3280A in cancer patients. Nature. 2014;515(7528):563-7.
7. Zhang J, Bu X, Wang H, Zhu Y, Geng Y, Nihira NT, et al. Cyclin D-CDK4 kinase destabilizes PD-L1 via cullin 3-SPOP to control cancer immune surveillance. Nature. 2018;553(7686):91-5.
8. Chung CH, Lin CY, Chen CY, Hsueh CW, Chang YW, Wang CC, et al. Ferroptosis Signature Shapes the Immune Profiles to Enhance the Response to Immune Checkpoint Inhibitors in Head and Neck Cancer. Adv Sci (Weinh). 2023:e2204514.
9. Jiao S, Xia W, Yamaguchi H, Wei Y, Chen MK, Hsu JM, et al. PARP Inhibitor Upregulates PD-L1 Expression and Enhances Cancer-Associated Immunosuppression. Clin Cancer Res. 2017;23(14):3711-20.
10. Bader JE, Voss K, Rathmell JC. Targeting Metabolism to Improve the Tumor Microenvironment for Cancer Immunotherapy. Mol Cell. 2020;78(6):1019-33.
11. Koundouros N, Poulogiannis G. Reprogramming of fatty acid metabolism in cancer. Br J Cancer. 2020;122(1):4-22.
12. Zhang Y, Kurupati R, Liu L, Zhou XY, Zhang G, Hudaihed A, et al. Enhancing CD8(+) T Cell Fatty Acid Catabolism within a Metabolically Challenging Tumor Microenvironment Increases the Efficacy of Melanoma Immunotherapy. Cancer Cell. 2017;32(3):377-91.e9.
13. Wu L, Zhang X, Zheng L, Zhao H, Yan G, Zhang Q, et al. RIPK3 Orchestrates Fatty Acid Metabolism in Tumor-Associated Macrophages and Hepatocarcinogenesis. Cancer Immunol Res. 2020;8(5):710-21.
14. Liu C, Chikina M, Deshpande R, Menk AV, Wang T, Tabib T, et al. Treg Cells Promote the SREBP1-Dependent Metabolic Fitness of Tumor-Promoting Macrophages via Repression of CD8(+) T Cell-Derived Interferon-$\gamma$. Immunity. 2019;51(2):381-97.e6.
15. Lai DW, Chu PY, Sheu ML, Tsai YC, Lee YH, Liu SC, et al. The potential immunotherapy effect of Ginkgolide B thwarts oral squamous cell carcinoma progression by targeting the SREBP1/KLK8/CCL22 axis. Phytomedicine. 2025;136:156249.
16. Zhang H, Li Y, Huang J, Shen L, Xiong Y. Precise targeting of lipid metabolism in the era of immuno-oncology and the latest advances in nano-based drug delivery systems for cancer therapy. Acta Pharm Sin B. 2024;14(11):4717-37.
17. Yin X, Xu R, Song J, Ruze R, Chen Y, Wang C, et al. Lipid metabolism in pancreatic cancer: emerging roles and potential targets. Cancer Commun (Lond). 2022;42(12):1234-56.
18. He Y, Qi S, Chen L, Zhu J, Liang L, Chen X, et al. The roles and mechanisms of SREBP1 in cancer development and drug response. Genes Dis. 2024;11(4):100987.
19. Fu Q, Chen Y, Huang D, Guo C, Zhang X, Xiao W, et al. Sintilimab Plus Modified FOLFIRINOX in Metastatic or Recurrent Pancreatic Cancer: The Randomized Phase II CISPD3 Trial. Ann Surg Oncol. 2023;30(8):5071-80.
20. Livak KJ, Schmittgen TD. Analysis of relative gene expression data using real-time quantitative PCR and the 2(-Delta Delta C(T)) Method. Methods. 2001;25(4):402-8.
21. Denkert C, Loibl S, Noske A, Roller M, Müller BM, Komor M, et al. Tumor-associated lymphocytes as an independent predictor of response to neoadjuvant chemotherapy in breast cancer. J Clin Oncol. 2010;28(1):105-13.
22. Zhang X, Huang X, Xu J, Li E, Lao M, Tang T, et al. NEK2 inhibition triggers anti-pancreatic cancer immunity by targeting PD-L1. Nat Commun. 2021;12(1):4536.
23. Chen X, Lu Y, Wang L, Ma X, Pu J, Lin L, et al. A fast chemical reprogramming system promotes cell identity transition through a diapause-like state. Nat Cell Biol. 2023;25(8):1146-56.
24. Lao M, Zhang X, Ma T, Xu J, Yang H, Duan Y, et al. Regulator of calcineurin 1 gene isoform 4 in pancreatic ductal adenocarcinoma regulates the progression of tumor cells. Oncogene. 2021;40(17):3136-3151.
25. Endo Y, Onodera A, Obata-Ninomiya K, Koyama-Nasu R, Asou HK, Ito T, et al. ACC1 determines memory potential of individual CD4(+) T cells by regulating de novo fatty acid biosynthesis. Nat Metab. 2019;1(2):261-75.
26. Kuipers RS, Luxwolda MF, Sango WS, Kwesigabo G, Velzing-Aarts FV, Dijck-Brouwer DA, et al. Postpartum changes in maternal and infant erythrocyte fatty acids are likely to be driven by restoring insulin sensitivity and DHA status. Med Hypotheses. 2011;76(6):794-801.
27. Martin-Perez M, Urdiroz-Urricelqui U, Bigas C, Benitah SA. The role of lipids in cancer progression and metastasis. Cell Metab. 2022;34(11):1675-99.
28. Sun Y, He W, Luo M, Zhou Y, Chang G, Ren W, et al. SREBP1 regulates tumorigenesis and prognosis of pancreatic cancer through targeting lipid metabolism. Tumour Biol. 2015;36(6):4133-41.
29. Zhou C, Qian W, Ma J, Cheng L, Jiang Z, Yan B, et al. Resveratrol enhances the chemotherapeutic response and reverses the stemness induced by gemcitabine in pancreatic cancer cells via targeting SREBP1. Cell Prolif. 2019;52(1):e12514.
30. Taube JM, Anders RA, Young GD, Xu H, Sharma R, McMiller TL, et al. Colocalization of inflammatory response with B7-h1 expression in human melanocytic lesions supports an adaptive resistance mechanism of immune escape. Sci Transl Med. 2012;4(127):127ra37.
31. Bertolio R, Napoletano F, Mano M, Maurer-Stroh S, Fantuz M, Zannini A, et al. Sterol regulatory element binding protein 1 couples mechanical cues and lipid metabolism. Nat Commun. 2019;10(1):1326.
32. Londregan AT, Wei L, Xiao J, Lintner NG, Petersen D, Dullea RG, et al. Small Molecule Proprotein Convertase Subtilisin/Kexin Type 9 (PCSK9) Inhibitors: Hit to Lead Optimization of Systemic Agents. J Med Chem. 2018;61(13):5704-18.
33. Liu X, Bao X, Hu M, Chang H, Jiao M, Cheng J, et al. Inhibition of PCSK9 potentiates immune checkpoint therapy for cancer. Nature. 2020;588(7839):693-8.
34. Sabatine MS. PCSK9 inhibitors: clinical evidence and implementation. Nat Rev Cardiol. 2019;16(3):155-65.

35. Liu H, Kuang X, Zhang Y, Ye Y, Li J, Liang L, et al. ADORA1 Inhibition Promotes Tumor Immune Evasion by Regulating the ATF3-PD-L1 Axis. Cancer Cell. 2020;37(3):324-39.e8.
36. Turbitt WJ, Buchta Rosean C, Weber KS, Norian LA. Obesity and CD8 T cell metabolism: Implications for anti-tumor immunity and cancer immunotherapy outcomes. Immunol Rev. 2020;295(1):203-19.
37. Liu X, Hartman CL, Li L, Albert CJ, Si F, Gao A, et al. Reprogramming lipid metabolism prevents effector T cell senescence and enhances tumor immunotherapy. Sci Transl Med. 2021;13(587):eaaz6314.
38. Lim SA, Su W, Chapman NM, Chi H. Lipid metabolism in T cell signaling and function. Nat Chem Biol. 2022;18(5):470-81.
39. Lim SA, Wei J, Nguyen TM, Shi H, Su W, Palacios G, et al. Lipid signalling enforces functional specialization of T(reg) cells in tumours. Nature. 2021;591(7849):306-11.
40. Liao P, Wang W, Wang W, Kryczek I, Li X, Bian Y, et al. CD8(+) T cells and fatty acids orchestrate tumor ferroptosis and immunity via ACSL4. Cancer Cell. 2022;40(4):365-78.e6.
41. Currie E, Schulze A, Zechner R, Walther TC, Farese RV, Jr. Cellular fatty acid metabolism and cancer. Cell Metab. 2013;18(2):153-61.
42. Ringel AE, Drijvers JM, Baker GJ, Catozzi A, García-Cañaveras JC, Gassaway BM, et al. Obesity Shapes Metabolism in the Tumor Microenvironment to Suppress Anti-Tumor Immunity. Cell. 2020;183(7):1848-66.e26.
43. Zhang C, Yue C, Herrmann A, Song J, Egelston C, Wang T, et al. STAT3 Activation-Induced Fatty Acid Oxidation in CD8(+) T Effector Cells Is Critical for Obesity-Promoted Breast Tumor Growth. Cell Metab. 2020;31(1):148-61.e5.
44. Yoo SK, Chowell D, Valero C, Morris LGT, Chan TA. Outcomes Among Patients With or Without Obesity and With Cancer Following Treatment With Immune Checkpoint Blockade. JAMA Netw Open. 2022;5(2):e220448.
45. Argilés JM, Busquets S, Stemmler B, López-Soriano FJ. Cancer cachexia: understanding the molecular basis. Nat Rev Cancer. 2014;14(11):754-62.
46. Gonçalves DC, Lira FS, Yamashita AS, Carnevali Junior LC, Eder R, Laviano A, et al. Liver lipid metabolism disruption in cancer cachexia is aggravated by cla supplementation -induced inflammation. Clin Nutr. 2019;38(5):2219-30.
47. Saitoski K, Ryaboshapkina M, Hamza GM, Jarnuczak AF, Berthault C, Carlotti F, et al. Proprotein convertase PCSK9 affects expression of key surface proteins in human pancreatic beta cells via intracellular and extracellular regulatory circuits. J Biol Chem. 2022;298(7):102096.
48. Almeida CR, Ferreira BH, Duarte IF. Targeting PCSK9: a promising adjuvant strategy in cancer immunotherapy. Signal Transduct Target Ther. 2021;6(1):111.
49. Yuan J, Cai T, Zheng X, Ren Y, Qi J, Lu X, et al. Potentiating CD8(+) T cell antitumor activity by inhibiting PCSK9 to promote LDLR-mediated TCR recycling and signaling. Protein Cell. 2021;12(4):240-60.
50. Guedeney P, Giustino G, Sorrentino S, Claessen BE, Camaj A, Kalkman DN, et al. Efficacy and safety of alirocumab and evolocumab: a systematic review and meta-analysis of randomized controlled trials. Eur Heart J. 2022 Feb 12;43(7):e17-e25.
51. Guedeney P, Sorrentino S, Giustino G, Chapelle C, Laporte S, Claessen BE, et al. Indirect comparison of the efficacy and safety of alirocumab and evolocumab: a systematic review and network meta-analysis. Eur Heart J Cardiovasc Pharmacother. 2021;7(3):225-35.
52. Koskinas KC, Windecker S, Pedrazzini G, Mueller C, Cook S, Matter CM, et al. Evolocumab for Early Reduction of LDL Cholesterol Levels in Patients With Acute Coronary Syndromes (EVOPACS). J Am Coll Cardiol. 2019;74(20):2452-62.

## SUPPORTING INFORMATION

Additional supporting information can be found online in the Supporting Information section at the end of this article.

**How to cite this article:** Lao M, Zhang X, Li Z, Sun K, Yang H, Wang S, et al. Lipid metabolism reprograming by SREBP1-PCSK9 targeting sensitizes pancreatic cancer to immunochemotherapy. Cancer Commun.. 2025;1–28. https://doi.org/10.1002/cac2.70038